UPPSALA
UNIVERSITET

Digital Comprehensive Summaries of Uppsala Dissertations from the Faculty of Science and Technology 1557

Searching for a charged Higgs boson and development of a hardware track trigger with the ATLAS experiment

JOAKIM GRADIN

ACTA
UNIVERSITATIS
UPSALIENSIS
UPPSALA
2017

ISSN 1651-6214
ISBN 978-91-513-0069-6
urn:nbn:se:uu:diva-329227

Dissertation presented at Uppsala University to be publicly examined in Häggsalen, Ångströmslaboratoriet, Lägerhyddsvägen 1, Uppsala, Friday, 27 October 2017 at 13:15 for the degree of Doctor of Philosophy. The examination will be conducted in English. Faculty examiner: Professor Susan Shotkin-Gascon (Institut de Physique Nucléaire de Lyon).

Abstract
Gradin, J. 2017. Searching for a charged Higgs boson and development of a hardware track trigger with the ATLAS experiment. *Digital Comprehensive Summaries of Uppsala Dissertations from the Faculty of Science and Technology* 1557. 110 pp. Uppsala: Acta Universitatis Upsaliensis. ISBN 978-91-513-0069-6.

This thesis describes searches for a heavy charged Higgs boson decaying into a top and bottom quark pair, and the development of a hardware track trigger with theATLAS experiment. The data for the two searches was collected with the ATLAS detector at the Large Hadron Collider(LHC) with pp collision energies of $\sqrt{s} = 8$ and 13 TeV, and corresponds to an integrated luminosity of 20.3 and 13.2 fb^{-1} respectively. The main background for this signal is the production of ft pairs with additional heavy flavor radiation. The searches with a single lepton in the final state found no evidence of a charged Higgs boson, and set 95% CL_S upper limits on the production times branching ratio for masses ranging between 200-1000 GeV. The preparation of using the final state with two leptons in future searches is discussed. The design of a hardware track trigger based on pattern matching and linear track fitting was studied for the purpose of reducing the high event rates of the High-Luminosity LHC, which is expected to provide pp collisions with a luminosity about five times the nominal value, in the second half of the 2020's. A simulation framework was developed to emulate the pattern matching and was used to test its ability to filter hits in high pile-up environments. The results of this simulation, together with simulations of the track fitting and latency, show that such a track trigger is a viable option for the ATLAS experiment in the High Luminosity-LHC era.

Keywords: High energy physics, charged Higgs boson, Particle tracking

Joakim Gradin, Department of Physics and Astronomy, High Energy Physics, Box 516, Uppsala University, SE-751 20 Uppsala, Sweden.

ISSN 1651-6214
ISBN 978-91-513-0069-6
urn:nbn:se:uu:diva-329227 (http://urn.kb.se/resolve?urn=urn:nbn:se:uu:diva-329227)

Dedicated to my family and friends

List of papers

This thesis is based on the following papers, which are referred to in the text by their Roman numerals.

I *The design of a fast level-1 track trigger for the high luminosity upgrade of ATLAS.*
Joakim Gradin on behalf of the ATLAS collaboration, PoS(LHCP2016)203, 2016.

II *Search for charged Higgs bosons in the $H^{\pm} \to tb$ decay channel in pp collisions at $\sqrt{s} = 8$ TeV using the ATLAS detector.*
The ATLAS Collaboration, Journal of High Energy Physics, 3, 2016.

III *Search for charged Higgs bosons in the $H^{\pm} \to tb$ decay channel in pp collisions at $\sqrt{s} = 13$ TeV using the ATLAS detector.*
The ATLAS Collaboration, CERN, ATLAS-CONF-2016-089, 2016

IV *Comparison of two hardware-based hit filtering methods in high-pileup environments*
J.Gradin, M.Mårtensson and R.Brenner, arXiv:1709.01034 [physics.ins-det], Submitted to Journal of Instrumentation, 2017

Reprints were made with permission from the publishers.

Contents

Introduction

"Nothing happens in contradiction to nature, only in contradiction to what we know of it. And that's a place to start. That's where the hope is."

Dana Scully, *The X-Files*

The Standard Model(SM) of particle physics has been very successful in describing experimental observations, including the discovery of a Higgs boson in 2012. However there are many questions that are left unanswered, e.g; What constitutes the observed dark matter? How did matter come to dominate over anti-matter in the universe? It is evident that the SM, in its current form, cannot be the full theory. The experiments at the Large Hadron Collider(LHC) at CERN are designed to test the SM predictions and search for new particles by examining the outcome of high energy particle collisions. Any observation of inconsistencies with the SM or the discovery of new particles would be crucial in the development of a more complete model.

Many theoretical extensions of the SM, that aim to answer the aforementioned questions, include more than one Higgs doublet, which would mean that the discovered Higgs boson is part of a larger family of particles. Among the additional particles in such a theory are charged scalar bosons, generally referred to as "charged Higgs bosons". The SM and the theoretical motivation for charged Higgs bosons are presented in Part I.

The ATLAS detector and the LHC are described in Part II. In the interest of maximizing the number of collisions seen by the experiments, the LHC will be upgraded around 2025. This means that the ATLAS detector in turn must be upgraded to handle the increased amount of data, as only a small fraction can be stored in the long term. The collision events that are stored for analysis are selected using "triggers", i.e. a series of hardware and software algorithms that examine the data immediately after the collision and decide if an event is of interest or not. The first stage uses hardware processors and must be able to make a decision at the time scale of microseconds. The development of a hardware trigger based on the information from particle trajectories is also presented in part II, along with a description of the planned upgrades of the LHC and the ATLAS detector.

The charged Higgs boson is expected to predominantly decay into a top and bottom quark pair, if the H^+ mass is large enough to allow

it. Searches for charged Higgs bosons produced in association with a top quark are discussed in part III. The two published searches, using 20.3 fb^{-1} 8 TeV and 13.2 fb^{-1} 13 TeV data, looked for charged Higgs bosons with a single lepton in the final state. Future analyses can benefit from including the final state with two leptons, the challenges of using this final state are also discussed in part III.

Author's contribution

This thesis is based on contributions to the ATLAS experiment in two areas; the search for a charged Higgs boson and the development of a hardware track trigger. Due to the nature of this experiment, with several thousand members, all results presented in this thesis are a collaborative effort. My personal contributions are summarized here.

For the studies on the hardware track trigger, I helped develop the simulation framework for the pattern matching logic(see chapter 6). This framework takes simulated events and builds banks of patterns corresponding to high p_{T} leptons. Using this framework I tested different settings for the banks, e.g number of detector layers, granularity of the superstrips and number of wildcards. The settings were optimized to meet the design requirements of the track trigger. The simulated performance of the trigger, using these pattern banks, was presented in Paper I. In Paper IV we studied the differences off two hit filtering methods, the pattern matching as developed for ATLAS and a method based on the Hough transform. For this paper I created a generic tracking detector simulation, using the Geant4 framework and a Pythia Monte Carlo simulation of proton-proton collisions, and tested the pattern matching method.

For the charged Higgs boson searches my main focus was on developing the analysis for the dilepton final state, but I also performed certain tasks for the single lepton final state analyses. For Paper II I trained Boosted Decision Trees(see section 8.5), which are used to classify an event as background- or signal-like. I evaluated the impact of the different input variables and options to train the BDT to get the best signal to background separation. For Paper III I processed the data and simulation samples, including systematical variations, to produce inputs for the fit. I made consistency checks between the data and simulation as well as with other people to make sure the results were trustworthy.

My work on the dilepton channel included; finding new variables that can separate the signal and background, developing a way to calculate the mass of the charged Higgs boson, processing samples, running the fits and limit extraction.

Other work that didn't directly lead to any publications but is part of the ATLAS detector operation and development include; The development of an xml/c++ interface used to build the geometry description of the pixel detector in inner detector layout studies. Using an existing code

base for the silicon strip detector,`GeoModelXml`, I implemented the pixel detector geometry as described in the Phase-II upgrade Letter of Intent. I also added the necessary c++ code to use the geometry in a Geant4 simulation. This geometry description was later used by other people working on layout studies for the detector upgrade. I also participated in the monitoring of the detector during data taking in the ATLAS control room at the inner detector station.

Part I:
Theory

1. The Standard Model of particle physics

The theory of the fundamental particles and their interactions are generally referred to as the Standard Model (SM) of particle physics. These fundamental particles make up ordinary matter[1] and account for the electromagnetic, strong and weak forces. The theory of the SM was gradually developed during the last century, with notable milestones such as the prediction and discovery of the antiparticle [1, 2], the quantum field theory of electrodynamics (QED), the Englert-Brout-Higgs (BEH) mechanism [3, 4, 5] and the unification of the electromagnetic and weak forces [6, 7, 8].

1.1 The particles of the standard model

A property of all elementary particles is that they carry "spin", an instrinic angular momentum. The spin is quantized in units of $\hbar/2$, i.e $s = n\hbar/2$ where n is an integer[2]. Particles with an odd or even n are called fermions or bosons respectively. Spinless particles, i.e $n = 0$, are called scalar bosons. No elementary particles with a spin higher than one has ever been observed. In the SM there are twelve types of fermions; six leptons and six quarks. There are four[3] gauge bosons and one scalar boson. The gauge bosons are sometimes referred to as "force carriers", since they mediate the fundamental forces; electromagnetic interactions involve photons, weak interactions the $W^{\pm}$ and Z^0 and the strong interactions are mediated by gluons. The leptons and quarks are usually divided into three generations ordered by their masses. Each lepton generation contains either an electron, a muon or a tau and the corresponding neutrino and each quark generation contains an up- and a down-type quark. The SM particles and some of their characteristic properties are shown in table 1.1.

Particle physics is most conveniently described using quantum field theory where the excitation of the fields are interpreted as the particles.

[1] I.e. stars, planets, animals et.c. excluding hypothetical matter such as "dark matter".
[2] $\hbar = h/2\pi$ is the reduced Plank constant.
[3] Formally, the W-boson carries electric charge and have two physical states with opposite charge, the gluons carry color charge and the interacting states form a "color octet" meaning that there are eight physical states.

Table 1.1. *The particles of the SM and some of their properties [9]. The masses are averages of experimental results.*

	Name	Symbol	Mass	Electric charge [e]	Spin [$\hbar$]
Leptons	electron neutrino	ν_e	< 2 eV	0	1/2
	muon neutrino	ν_μ	< 0.19 MeV	0	1/2
	tau neutrino	ν_τ	< 18.2 MeV	0	1/2
	electron	e	0.511 MeV	-1	1/2
	muon	μ	105.7 MeV	-1	1/2
	tau	τ	1.777 GeV	-1	1/2
Quarks	up	u	2.2 MeV	$+2/3$	1/2
	down	d	4.7 MeV	$-1/3$	1/2
	charm	c	1.27 GeV	$+2/3$	1/2
	strange	s	96 MeV	$-1/3$	1/2
	top	t	173 GeV	$+2/3$	1/2
	bottom	b	4.18 GeV	$-1/3$	1/2
Bosons	gluon	g	0	0	1
	photon	γ	0	0	1
	W-boson	$W^\pm$	80.4 GeV	± 1	1
	Z-boson	Z^0	91.2 GeV	0	1
	Higgs boson	H	125 GeV	0	0

Using a Lagrangian formalism, the basis of all physics can be described with a Lagrange density often referred to as the Lagrangian

$$\mathcal{L} = \mathcal{L}(\phi_i(x), \partial_\mu \phi_i(x)), \tag{1.1}$$

where $\phi_i(x)$ are the fields described by the theory. Requiring that the Lagrangian is gauge invariant (i.e there is at least one redundant degree of freedom, and changing this gauge does not affect the physical content of the theory) gives rise to gauge fields and by Noethers theorem each gauge symmetry has an associated conserved charge. In the development of the SM this requirement has yielded accurate descriptions of the observed electromagnetic, weak and strong interactions.

For a theory to preserve special relativity, the fields must transform as a representation of the Poincaré group, i.e. the group of Lorentz transformations and translations. For spin 1/2 fields there are two possibilities, a "left-" or "right-handed" representation. The SM fermion fields can be decomposed into left handed and right handed components, the particles are then said to have a specific handedness, or "chirality".

An $\mathrm{SU}(2)_L \times \mathrm{U}(1)_Y$ gauge symmetry, where the subscript L refers to that the SU(2) symmetry applies to the left-handed components of the fields and Y is the "weak hypercharge" carried by all fermions, is the basis for the electromagnetic and weak (EW) interactions. Since SU(2) is same symmetry group associated with ordinary spin, the quantum num-

ber associated to $\mathrm{SU}(2)_L$ is called "weak isospin"(I) although it is not a physical angular momentum. In the weak isospin basis the fermion fields can be arranged in right handed singlets and left handed doublets

$$l_L^i = \begin{pmatrix} \nu_L^i \\ l_L^i \end{pmatrix}, \; q_L^i = \begin{pmatrix} u_L^i \\ d_L^i \end{pmatrix}, \tag{1.2}$$

where i stands for the three lepton and quark generations. Note that in this model there are no right handed neutrinos. As is, this model contains four massless gauge bosons, $A_\mu^{1,2,3}$ and B_μ, which through the BEH mechanism described in the next section mix to form the physical gauge bosons of the EW theory. Another consequence of this mechanism is that the originally conserved charges are also mixed and the remaining conserved charge is the electrical charge $Q = I_3 + Y/2$ where I_3 is the third component of the weak isospin.

Quarks and gluons have an additional color charge which comes in tree colors obeying a SU(3) gauge group structure. The potential of the strong force differs from those of the other fundamental forces in that it has a minimum; at short range $V_{strong} \propto 1/r$ while at long range $V_{strong} \propto r$. At short ranges the color charged particles can form bound states. The behavior of the potential at long range has the consequence that a colored particle cannot be observed directly. E.g. for a quark-antiquark pair produced in a pp collision, there will at a certain distance between the two particles be enough energy in the system that a new particle pair can be "extracted" from the vacuum, forming two color neutral bound states. Depending on the initial energy of the states this can continue in a cascading fashion, referred to as hadronization. In a high energy experiment one sees "jets" of many particles with a combined energy and direction proportional to that of the initial quark or gluon. The bound states of quarks are known as "hadrons", the proton is a hadron with three valence quarks (uud). Although theoretically possible, bound states of gluons have not been confirmed experimentally.

All electrically charged particles have an antiparticle with opposite charge. The photons and the Z boson are considered their own antiparticles, while the nature of the neutral fermions of the SM, the neutrinos, is somewhat unknown. Neutrinos have only been observed with left handed chirality, suggesting that they are massless, however we know from their oscillations [10, 11] that they do have mass. The origin of the neutrino masses is an open question and one reason for searching for physics beyond the SM.

1.2 Particle masses and the Higgs boson

The theory of the EW interaction has a $\mathrm{SU}(2)_L \times \mathrm{U}(1)_Y$ symmetry with four massless gauge bosons. In the 1960's several people showed that massive gauge bosons can emerge through the process of spontaneous symmetry breaking [3, 4, 5]. This concept was then applied to the EW theory, where the result is the physical W and Z bosons and the massless photon. The following description of the EW symmetry breaking is based on the one in [12]. The SM $\mathrm{SU}(2)_L \times \mathrm{U}(1)_Y$ gauge symmetry can be spontaneously broken by a complex scalar doublet

$$\phi = \begin{pmatrix} \phi^+ \\ \phi^0 \end{pmatrix}. \tag{1.3}$$

with $Y = 1$. The Lagrangian for this field is

$$\mathcal{L}_\phi = |D_\mu \phi|^2 - V(\phi) \tag{1.4}$$

The gauge bosons will acquire a mass if this field has a non-zero vacuum expectation value (VEV). The scalar potential

$$V(\phi) = -\mu^2 \phi^\dagger \phi + \frac{\lambda}{2}(\phi^\dagger \phi)^2 \tag{1.5}$$

will have a minimum at

$$\phi^\dagger \phi = \frac{\mu^2}{2\lambda}. \tag{1.6}$$

By giving the VEV the form

$$\langle \phi(x) \rangle = \frac{1}{\sqrt{2}} \begin{pmatrix} 0 \\ v \end{pmatrix} \tag{1.7}$$

it will minimize $V(\phi)$ while also conserving electrical charge. This form can be achieved by a rotation in the SU(2) basis without changing the physics. The covariant derivative in equation 1.4 is

$$D_\mu \phi = (\partial_\mu - \frac{ig}{2} A_\mu^a \sigma^a - i\frac{1}{2} g' B_\mu)\phi, \tag{1.8}$$

where σ^a are the Pauli matrices, a = 1,2,3, and g and g' are the coupling constants for the gauge bosons. By evaluating equation 1.4 at the VEV we can identify the physical states

$$W_\mu^\pm = \frac{1}{\sqrt{2}}(A_\mu^1 \mp i A_\mu^2) \quad \text{with} \quad m_W = g\frac{v}{2}, \tag{1.9}$$

$$Z_\mu^0 = \frac{1}{\sqrt{g^2 + g'^2}}(g A_\mu^3 - g' B_\mu) \quad \text{with} \quad m_Z = \sqrt{g^2 + g'^2}\frac{v}{2} \tag{1.10}$$

and

$$A_\mu = \frac{1}{\sqrt{g^2+g'^2}}(gA^3_\mu + g'B_\mu) \quad \text{with} \quad m_A = 0. \tag{1.11}$$

Here the massive W and Z bosons have emerged from the theory together with the vector field A_μ with a massless gauge boson, the photon. It is possible to parameterize the Higgs doublet in the form

$$\phi = \mathrm{U}(x)\begin{pmatrix} 0 \\ (v+h(x))/\sqrt{2} \end{pmatrix} \tag{1.12}$$

where $\mathrm{U}(x)$ is a local SU(2) gauge transform and $h(x)$ is a scalar field with $\langle h(x) \rangle = 0$. The gauge can be fixed so that the transformation is the identity. Using this parameterization the results above hold and a new massive scalar boson, the Higgs boson (h) with $m_h = \sqrt{2\lambda}v$, is manifest in the theory. This means that three of the doublet's four degrees of freedom have been used to form the massive EW gauge bosons. The naive way to describe the mass of the fermions would be to insert a term of the form $-m_f \bar{f} f$, where f is any of the charged fermion fields, in the Lagrangian. However, the SU(2) symmetry only applies to left handed particles and thus

$$-m_f \bar{f} f = -m_f(\bar{f}_R f_L + \bar{f}_L f_R) \tag{1.13}$$

is not gauge invariant. Instead, one can introduce a gauge invariant Yukawa coupling to the Higgs field,

$$-\lambda_f \bar{f}_L h f_R, \tag{1.14}$$

which can be rewritten using 1.13 as

$$-\frac{\lambda_f v}{\sqrt{2}}\bar{f} f - \frac{\lambda_f}{\sqrt{2}} h \bar{f} f, \tag{1.15}$$

where the fermions have gained their mass $m_f = \lambda_f v/\sqrt{2}$ and a fermion-Higgs interaction has been introduced. The coupling constant, λ_f, is dependent on the fermion type. The part of the SM Lagrangian that concerns the Higgs field interactions with the standard model particles is, at leading order,

$$\mathcal{L}_{Higgs} = \frac{2m_W^2}{v}\overline{W}Wh + \frac{m_Z^2}{v}Z^2 h - \frac{m_f}{v}\bar{f} f h - m_h^2 h^\dagger h + \frac{v^2}{2m_h}(h^\dagger h)^2. \tag{1.16}$$

The Higgs boson thus couples to all the massive particles of the SM, including itself, with a coupling strength proportional to the particle mass. At the LHC the Higgs boson is predominantly produced via gluon fusion through a top quark loop, in the context of this thesis the most important

production mode is $t\bar{t}H$ as with $H \to b\bar{b}$ it is one of the irreducible backgrounds for a $H^{\pm} \to tb$ signal . Feynman diagrams for these processes are shown in figure 1.1. The production cross section and branching ratios are shown in figures 1.2 and 1.3.

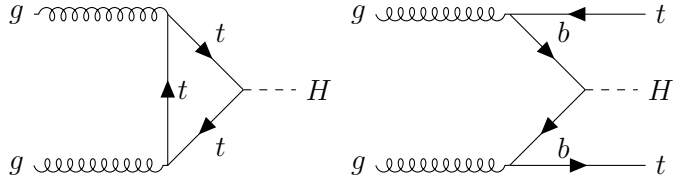

Figure 1.1. Feynman diagrams of SM Higgs production via a top quark loop (left) and in association with a $t\bar{t}$ pair (right).

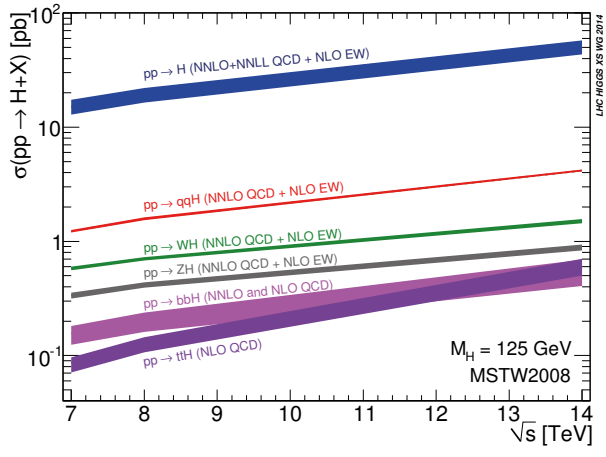

Figure 1.2. The production cross section of the SM Higgs boson as function of the LHC center of mass energy. [13]

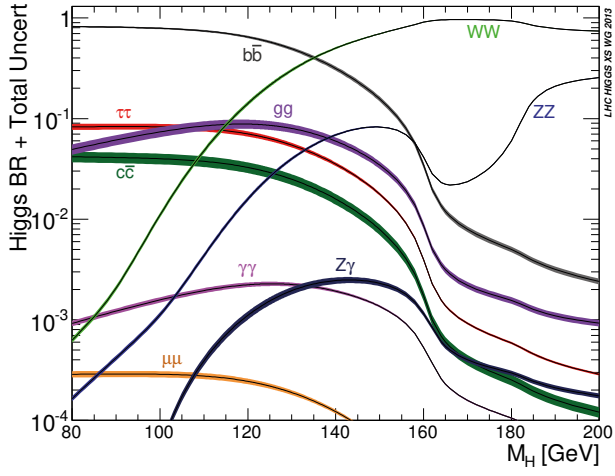

Figure 1.3. The branching ratios of the SM Higgs boson as function of mass. [14]

2. Physics beyond the standard model

The SM has proved to be very successful with many predictions later verified experimentally, e.g the discoveries of the W and Z bosons [15, 16, 17, 18] and a Higgs boson [19, 20] at CERN. However, there are some fundamental problems that the SM doesn't explain. The SM does not include gravity and a quantized theory of gravity that agrees with general relativity has not been found. Astronomical observations of gravitational effects have shown the existence of "dark matter", i.e matter that does not interact with photons, which cannot be explained by any of the SM particles. If the dark matter consist of particles that do, in some way, interact with the SM particles there is a possibility they can be produced at the LHC. The SM does not explain the phenomena of neutrino oscillations, an observed effect that show that a neutrino of one flavor will oscillate into another flavor if propagating freely. These are some of the reasons for the development of Beyond the Standard Model (BSM) theories.

One popular theory is "supersymmetry", or SUSY, where a symmetry is imposed on the spin. In a SUSY theory all the fermions have bosononic superpartners (labled "squarks" and "sleptons") and the bosons have fermionic partners (Winos, Binos, gluinos and Higgsinos). In such a model one has to introduce a second Higgs doublet, resulting in several Higgs bosons. A nice feature of supersymmetric theories are that they can resolve what is known as the hierarchy problem or the fine tuning of the Higgs mass. The measured mass of the Higgs boson (i.e ≈ 125 GeV) is a sum of the bare mass and quantum loop corrections. The loop corrections are proportional to the Higgs couplings with the SM particles and a cutoff scale to keep the loop integration from diverging. If one assumes the SM to be an effective theory[1], and that it will stop being valid at some scale, the corrections can be assumed to be proportional to this scale. Since there are no indications that the SM is invalid for the energy scales of current experiments the order of this cutoff can be anywhere from a few TeV up to the Plank scale, 10^{16} TeV. Considering that the mass of the Higgs boson has been measured to such a low value, there must be something that cancels these large corrections. In a supersymmetric model the couplings to the superpartners will contribute to the Higgs boson mass with the opposite sign of their SM equivalents, and exactly cancel

[1] If the SM is considered the complete theory the scale cutoff (and thus the measureable Higgs boson mass) goes to infinity.

the corrections if the SM particles and the superpartners have the same mass. However, we know that this is not true as they would have been seen in experiments along with the SM particles. A Higgs boson mass of 125 GeV can still be accommodated for if supersymmetry is broken at the TeV scale, which would mean that the superpartners should have masses accessible at the LHC.

2.1 Two Higgs doublet models

The next simplest symmetry breaking term from a single field is two doublets, e.g

$$\phi_1 = \begin{pmatrix} \phi_1^0 \\ \phi_1^- \end{pmatrix} \quad \text{and} \quad \phi_2 = \begin{pmatrix} \phi_2^+ \\ \phi_2^0 \end{pmatrix}. \tag{2.1}$$

The scalar potential of these doublets can be very cumbersome and has 14 parameters, it can be simplified (and more testable) with some assumptions [21]. A global Z_2 symmetry ($\phi_1 \to \phi_1, \phi_2 \to -\phi_2$) will ensure that charge-parity (CP) is conserved and a potential which in general conserves CP can be written as

$$\begin{aligned} V(\phi_1,\phi_2) = {} & m_{11}^2\phi_1^\dagger\phi_1 + m_{22}^2\phi_2^\dagger\phi - m_{12}^2(\phi_1^\dagger\phi_2 - \phi_2^\dagger\phi_1) \\ & + \frac{\lambda_1}{2}(\phi_1^\dagger\phi_1)^2 + \frac{\lambda_2}{2}(\phi_2^\dagger\phi_2)^2 + \lambda_3\phi_1^\dagger\phi_1\phi_2^\dagger\phi_2 \\ & + \lambda_4\phi_1^\dagger\phi_1\phi_2^\dagger\phi_2 + \frac{\lambda_5}{2}[(\phi_1^\dagger\phi_2)^2 + (\phi_2^\dagger\phi_1)^2] \end{aligned} \tag{2.2}$$

where m_{ij}^2 and λ_x are real parameters. It should be noted that $m_{12}^2(\phi_1^\dagger\phi_2 - \phi_2^\dagger\phi_1)$ is the term that breaks the Z_2 symmetry and allows for CP-violating transitions. However the symmetry is only softly broken, i.e the effects vanish at small distances [22]. This potential can be minimized with

$$\langle\phi_1\rangle = \begin{pmatrix} 0 \\ \frac{v_1}{\sqrt{2}} \end{pmatrix} \quad \text{and} \quad \langle\phi_2\rangle = \begin{pmatrix} 0 \\ \frac{v_2}{\sqrt{2}} \end{pmatrix}. \tag{2.3}$$

These doublets can be used to achieve the EW symmetry breaking in a way similar to that described in section 1.2 with the notable exception that the theory is left with not one but five Higgs bosons; two neutral scalars, h and H, a neutral pseudo-scalar A and two charged scalars $H^\pm$. As in the SM version of the EW symmetry breaking the doublets can be parametrized by real-valued fields:

$$\phi_{1,2} = \begin{pmatrix} \phi_{1,2}^+ \\ (v_{1,2} + \rho_{1,2} + i\eta_{1,2})/\sqrt{2} \end{pmatrix} \tag{2.4}$$

where ϕ^+, ρ and η are massless charged scalar, neutral scalar and neutral pseudo-scalar fields respectively. The mass terms for the charged fields are

$$\mathcal{L}_{\phi^\pm mass} = [m_{12}^2 - (\lambda_4+\lambda_5)v_1v_2](\phi_1^-, \phi_2^-) \begin{bmatrix} \frac{v_2}{v_1} & -1 \\ -1 & \frac{v_1}{v_2} \end{bmatrix} \begin{pmatrix} \phi_1^+ \\ \phi_2^+ \end{pmatrix}. \tag{2.5}$$

To find the physical states, that is mass eigenstates, the matrix must be diagonalized. This can be done with a rotation by an angle β such that $M_{diag} = R(\beta)^T M R(\beta)$ where R is a 2×2 rotation matrix. This particular matrix will be diagonalized if $\tan\beta$ is taken to be the ratio of the two VEVs v_2/v_1, in addition one of the eigenvalues (i.e one mass squared term) is zero. Inserting $R(\beta)R(\beta)^T$ on each side of the matrix in equation 2.5 we can read off the physical fields as

$$R(\beta)^T \begin{pmatrix} \phi_1^+ \\ \phi_2^+ \end{pmatrix} = \begin{pmatrix} \cos(\beta)\phi_1^+ + \sin(\beta)\phi_2^+ \\ -\sin(\beta)\phi_1^+ + \cos(\beta)\phi_2^+ \end{pmatrix} = \begin{pmatrix} G^+ \\ H^+ \end{pmatrix} \tag{2.6}$$

where G^+ is a massless Goldstone boson and H^+ is a massive charged Higgs boson. The definition of the charge conjugate states is identical. The mass terms for the pseudo scalar fields are

$$\mathcal{L}_{\eta mass} = [\frac{m_{12}^2}{v_1v_2} - 2\lambda_5](\eta_1, \eta_2) \begin{bmatrix} v_2^2 & -v_1v_2 \\ -v_1v_2 & v_1^2 \end{bmatrix} \begin{pmatrix} \eta_1 \\ \eta_2 \end{pmatrix}. \tag{2.7}$$

This matrix is also diagonalized by a rotation β. The resulting fields are one massive and one massless pseudo-scalar:

$$R(\beta)^T \begin{pmatrix} \eta_1 \\ \eta_2 \end{pmatrix} = \begin{pmatrix} \cos(\beta)\eta_1 + \sin(\beta)\eta_2 \\ -\sin(\beta)\eta_1 + \cos(\beta)\eta_2 \end{pmatrix} = \begin{pmatrix} G^0 \\ A \end{pmatrix}. \tag{2.8}$$

The $G^\pm$ and G^0 will provide the degrees of freedom to generate the massive $W^\pm$ and Z bosons in the EW symmetry breaking. Lastly, the neutral fields have mass terms

$$\mathcal{L}_{\rho mass} = -(\rho_1, \rho_2) \begin{bmatrix} m_{12}^2\frac{v_2}{v_1} + \lambda_1 v_1^2 & -m_{12}^2 + \lambda_{345}v_1v_2 \\ -m_{12}^2 + \lambda_{345}v_1v_2 & m_{12}^2\frac{v_1}{v_2} + \lambda_2 v_2^2 \end{bmatrix} \begin{pmatrix} \rho_1 \\ \rho_2 \end{pmatrix}. \tag{2.9}$$

This matrix can be diagonalized by an angle α and results in two neutral Higgs bosons:

$$-R(\alpha)^T \begin{pmatrix} \rho_1 \\ \rho_2 \end{pmatrix} = \begin{pmatrix} -\cos(\alpha)\rho_1 - \sin(\alpha)\rho_2 \\ \sin(\alpha)\rho_1 - \cos(\alpha)\rho_2 \end{pmatrix} = \begin{pmatrix} H \\ h \end{pmatrix} \tag{2.10}$$

where the minus sign is needed to give the mass term the right sign and h is the lighter of the two. These neutral Higgs bosons take the role of the SM Higgs boson as a linear combination

$$H_{SM} = h\sin(\alpha-\beta) - H\cos(\alpha-\beta). \tag{2.11}$$

The light boson, h, is usually assumed to be the 125 GeV boson observed in experiments, in the limit $\cos(\alpha - \beta) = 0$ it behaves like the SM Higgs boson. For the purpose of testing 2HDMs in experiments, it is much more convenient to parameterize the potential, equation 2.2, using the Higgs masses, the mixing angles α and β and m_{12}. These seven parameters make for a rather large parameter space for a 2HDM. However, interpreting the observed boson as one of the neutral Higgs bosons and measurements of its couplings will introduce some constraints, see e.g [23].

The 2HDMs will in general allow flavor changing neutral currents (FCNC) at tree level. As these currents would introduce effects that are not experimentally observed it is desirable to construct a theory without FCNC. It has been demonstrated in [24] that for fermions in a $\mathrm{SU}(2) \times \mathrm{U}(1)$ gauge theory, the flavor will be conserved if all fermions of a certain charge and chirality have the same value of I_3 and receive their mass term from a single source. Assuming a SM like fermion sector, these conditions are fulfilled if the right handed fermions with the same charge couple only to one Higgs doublet. This results in four different models, shown in table 2.1, depending on which doublet the up and down quarks and charged leptons couple to. The up type quarks are always coupled to ϕ_2 by convention.

Table 2.1. *The 2HDM types are defined by which Higgs doublet couples to the up-, down-quarks and the leptons [21].*

Model	u^i_R	d^i_R	l^i_R
Type I	ϕ_2	ϕ_2	ϕ_2
Type II	ϕ_2	ϕ_1	ϕ_1
Lepton specific	ϕ_2	ϕ_2	ϕ_1
Flipped	ϕ_2	ϕ_1	ϕ_2

The Minimal Supersymmetric Model (MSSM), implies a type-II 2HDM. In addition the parameters of the quartic terms in the Higgs potential (i.e λ_i in equation 2.2) can be expressed in terms of the Gauge boson masses. Thus, at tree level the MSSM can be parameterized using only two parameters, usually $\tan(\beta)$ and the mass of the most relevant BSM Higgs boson. However, to take higher order corrections, which can have sizeable effects on the particle masses, into account one can use one of the many benchmark scenarios. Among the most popular ones are the m_h^{max}, m_h^{mod+} and m_h^{mod-} scenarios. The m_h^{max} scenario was devised to maximize the lightest neutral Higgs boson and is mostly excluded after the discovery of a 125 GeV boson, the $m_h^{mod\pm}$ are modified versions that allow for a 125 GeV h by reducing the stop corrections to the h mass [25].

2.2 Charged Higgs boson phenomenology

The Higgs bosons of a 2HDM will couple to the SM fermions through Yukawa couplings. A general Yukawa Lagrangian for the four types in table 2.1 is

$$\begin{aligned}\mathcal{L}_{Yukawa}^{2HDM} = &-\sum_{f=u,d,l}\frac{m_f}{v}(\xi_h^f\bar{f}fh+\xi_H^f\bar{f}fH-i\xi_A^f\bar{f}\gamma_5 f)\\ &-\left\{\frac{\sqrt{2}V_{ud}}{2}\bar{u}(m_u\xi_A^u P_L+m_d\xi_A^d P_R)dH^+\right.\\ &\left.+\frac{\sqrt{2}}{v}m_l(\xi_A^l\bar{\nu_l}l_R H^+)+H.C\right\}\end{aligned} \tag{2.12}$$

where $v=\sqrt{v_1^2+v_2^2}$, $P_{L,R}$ are left/right projection operators and ξ_ϕ^f are functions of α and β [26]. The factors ξ_ϕ^f are dependent on the 2HDM type, the ones of interest for the charged Higgs couplings are shown in table 2.2. In a type I model the coupling to the fermions have the same magnitude and H^+ will be fermiophobic at large $\tan(\beta)$, i.e the couplings become very small. In a lepton specific model the quark couplings decrease while the lepton couplings increase with $\tan(\beta)$. This means that searches for a charged Higgs produced or decaying through quark interaction will have limited sensitivity at high $\tan(\beta)$ in these two models.

Table 2.2. *The 2HDM type specific factors for the charged Higgs boson Yukawa couplings to the SM fermions.*

Model	ξ_A^u	ξ_A^d	ξ_A^l
Type I	$\cot(\beta)$	$-\cot(\beta)$	$-\cot(\beta)$
Type II	$\cot(\beta)$	$\tan(\beta)$	$\tan(\beta)$
Lepton specific	$\cot(\beta)$	$-\cot(\beta)$	$\tan(\beta)$
Flipped	$\cot(\beta)$	$\tan(\beta)$	$-\cot(\beta)$

The fermion masses are also important for the couplings and, in general, $H^+\to tb$ or $H^+\to\tau\nu$ is the dominant decay mode when m_{H^+} is higher or lower than the top quark mass respectively. The branching ratios in the m_h^{max} and $m_h^{mod\pm}$ scenarios are shown in figure 2.1. The dominant production mode of a charged Higgs boson at the LHC would be through a tb vertex, when calculating the cross section two approaches are used; the four flavor scheme (4FS) and five flavor scheme (5FS). The difference is that in the 5FS the b quark is included in the parton density function of the proton and considered massless in relation to the hard scatter energy scale, whereas in the 4FS it is produced via gluon-splitting and massive. The Feynman diagrams for these processes are shown in figure 2.2. The two schemes yield slightly different numbers and are combined using the "santander matching" [27] method. The combined cross

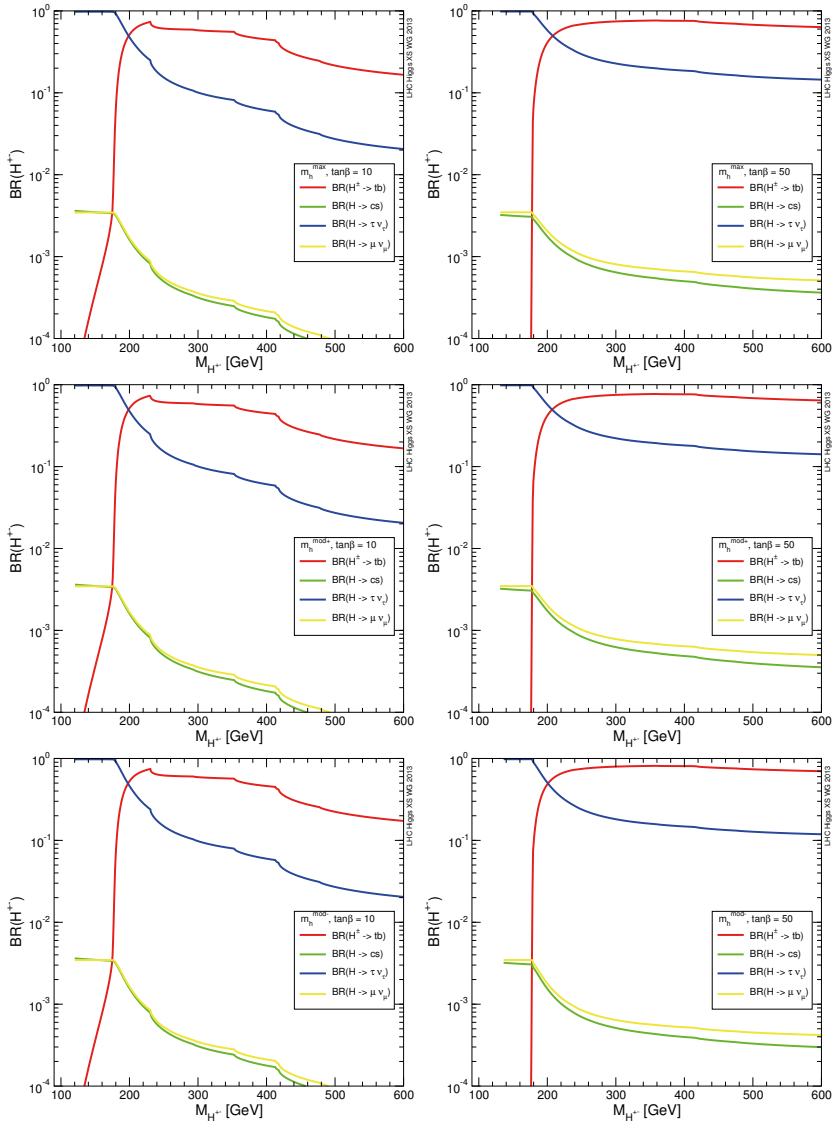

Figure 2.1. The branching ratio of the charged Higgs boson in the m_h^{max} and $m_h^{mod\pm}$ benchmark scenarios of the MSSM. The kinks in the curves correspond to when the decays to supersymmetric particles (not included in the plots) become kinematically allowed. [13]

section is then used when interpreting results and producing exclusion plots. The charged Higgs production cross section as a function of mass and tan(β) is shown in figure 2.3.

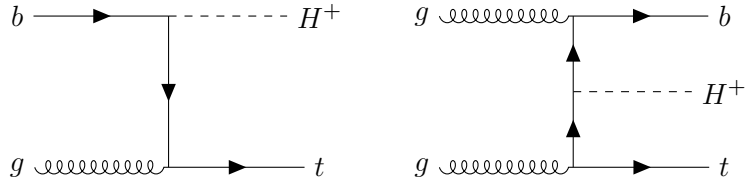

Figure 2.2. The production of a charged Higgs boson in the five flavor scheme (left) and four flavor scheme (right).

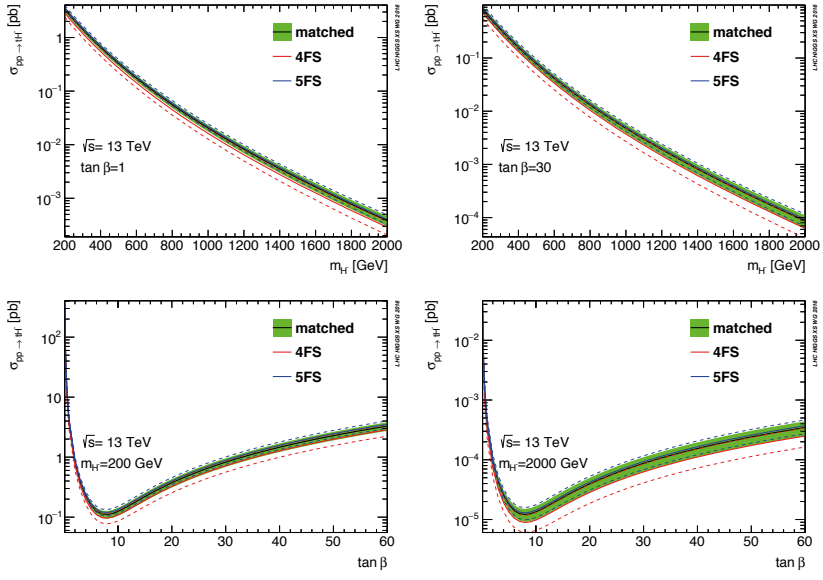

Figure 2.3. The production cross section of charged Higgs bosons as functions of $m_{H^\pm}$ or tan(β). [13]

Part II:
The ATLAS experiment at the Large Hadron Collider

3. The Large Hadron Collider

The Large Hadron Collider (LHC) is a circular collider housed at CERN near Geneva, Switzerland [28]. It provides high energy particle collisions for several experiments including the general purpose detectors ATLAS [29] and CMS [30], the b-physics oriented LHCb [31] and the heavy ion centered ALICE [32]. The LHC ring is 27 km long and situated almost 100 meters underground. Two beams of either protons or lead nuclei travel in opposite directions of the ring and intersect at four different interaction points, where the collisions occur. The particles in the beams are guided by superconducting electromagnets placed in sections around the ring. The main magnets are dipoles with a field strength of more than 8 Tesla that keep the particles on a circular orbit. There are also many types of magnets that correct drifts in the particle trajectories and focus the beams at the interaction points.

The protons are accelerated in stages in a Linear accelerator and a series of synchrotron rings before they are injected into the LHC. Upon injection the protons have an energy of 450 GeV and the LHC then brings them up to the collision energy. A schematic view of the LHC and the preceding stages is shown in figure 3.1. During the data taking period in 2011-2012, "run I", the protons collided with a center of momentum energy $\sqrt{s} = 7$ and later 8 TeV. Since 2015, in "run II", the energy was increased to 13 TeV.

Radiofrequency cavities are used to accelerate the protons and keep them in bunches via an oscillating electromagnetic field. The oscillations are timed so that a proton with a nominal revolution frequency will not be accelerated further, while a proton with a higher or lower frequency will be accelerated or decelerated. This has the effect that the protons will oscillate around the nominal bunch position as they travel around the ring. The distribution of the protons around this nominal position is characterized by the emmittance, ε, the spread in the momentum-position phase space. The bunches have an emmittance along the beam direction but also in the transverse plane due to effects from gravity and focusing magnets. Each bunch contains about 10^{11} protons and the LHC is designed to be loaded with 2808 bunches at a 25 ns spacing.

The number of expected collision events can be expressed as

$$N = \sigma \int L dt \tag{3.1}$$

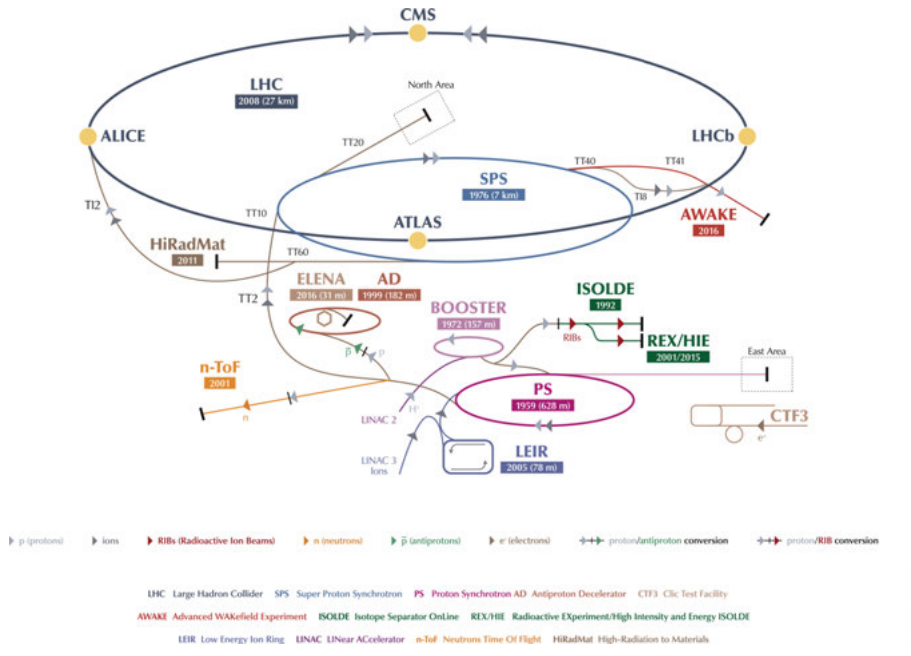

Figure 3.1. The CERN accelerator complex. [33]

where σ is the cross section of the physical process and L is the instantaneous luminosity, which is integrated over the data collection time. The cross section is most commonly expressed in the unit barn(b) where $1\text{b} = 10^{-24}$ cm^2. The integrated luminosity then has the unit b^{-1}. While the cross section is dependent on the physical process at hand, the luminosity is dependent on the beam parameters:

$$L = \frac{fN^2 k_b}{A_{eff}} F \tag{3.2}$$

where f is the revolution frequency, N is the number of protons per bunch, k_b is the number of bunches, A_{eff} is the effective cross sectional area of the colliding bunches and F is a geometrical factor due to the crossing angle. For two bunches colliding head on the effective area is $4\pi\sigma_x\sigma_y$, where $\sigma_{x,y}$ is the RMS of the proton distributions in the transverse plane for the bunches. At the LHC the area is usually expressed as

$$A_{eff} = \varepsilon\beta^*/\gamma, \tag{3.3}$$

where γ is the relativistic factor and β^* is a measurement of how focused the beam is at the interaction point. A value of $\beta^* = 1$ m would mean that the beam width doubles 1 m away from the interaction point.

At the LHC the luminosity is high enough to make it probable for more than one collision per bunch crossing, there is a so called pile-up of

collisions. The expected number of collisions per bunch crossing, denoted by μ, is calculated by

$$\mu = \frac{\sigma_{in} L}{k_b f}, \tag{3.4}$$

where σ_{in} is the cross section for inelastic pp collisions. Elastic collisions, where the protons scatter without breaking up, are in general not visible in ATLAS due to the small scattering angles. The majority of the pile-up collisions are "soft QCD" events, e.g. processes involving the lightest quarks and final states with low transverse momentum particles. Since any candidate event for a search will most probably be accompanied by several pile-up collisions it is important to measure this background. ATLAS measures pile-up interactions using so called "minimum bias" triggers which selects random bunch crossings with at least a few hits in the detector. This data set is then used to check and correct the modeling of pile-up events for simulated data. The mean number of pile-up events per bunch crossing during run I and II are shown in figure 3.2.

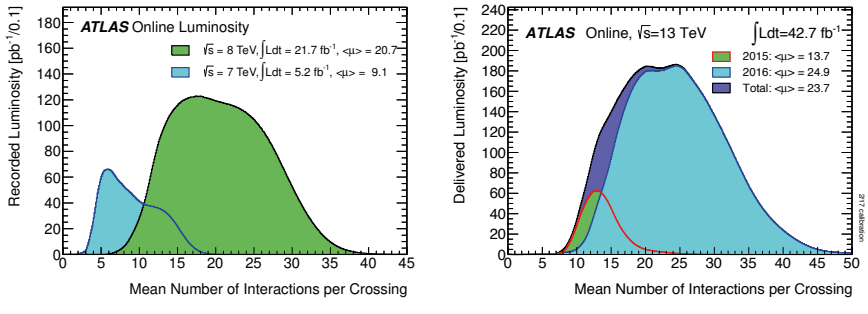

Figure 3.2. The mean number of pile-up events in run I [34] (left) and run II [35] (right).

4. The ATLAS detector

The ATLAS (A Toroidal LHC ApparatuS) detector [29], shown in figure 4.1, is situated at one of the four interaction points of the LHC and is comprised of four main components; The inner detector, the calorimeters, the muon spectrometer, and the magnet system, which will be described in the following sections. The Trigger and Data Acquisition (TDAQ) system is also an important part of the detector, as it is resposible for selecting the events to store for analysis and transfer data from the detector. The detector is generally divided into a "barrel" section, a cylindrical volume centered at the interaction point, and an "endcap" at either side. The ATLAS coordinate system is defined as right handed with origin at the interaction point, $\hat{z}$ along the beam axis and $\hat{x}$ pointing at the center of the LHC ring. More commonly, cylindrical coordinates are used, specified by the radial distance to the z-axis, the azimuthal angle ϕ in the transverse plane. Instead of the polar angle θ it's often more suitable to use the pseudorapidy, $\eta = -\ln(\tan(\theta/2))$. The distance, $\Delta\eta$, is Lorentz invariant under boosts along the beam line. This property is useful at a hadron colliders since the partons, e.g. quarks and gluons in a proton, carry fractions of the total proton momentum and thus have unknown longitudinal momenta. E.g. the center of mass frame for an interaction can be boosted along z with respect to the experimental frame, if that event contains for example two leptons the $\Delta\eta$ between them is the same in the interaction frame as the lab frame. Another useful quantity is the distance between two points in the η-ϕ plane $\Delta R = \sqrt{(\Delta\phi)^2 + (\Delta\eta)^2}$. The fact that the partons longitudinal momentum is unknown also means that the sum of momenta for all final state particles does not have to be zero. However, the transverse momentum of the partons is generally much lower than for the particles created in a hard scattering event. Thus the total transverse momentum sum is assumed to be zero. Although energy is a scalar quantity, a transverse energy E_{T} is often used at hadron colliders for the same reason as p_{T}. It is defined as $E_{\mathrm{T}} = E\sin(\theta)$, where E is the energy measured in a calorimeter cell and θ is the polar angle of a vector pointing to that cell.

4.1 The Inner Detector

The Inner Detector(ID) [37] is, as its name suggests, the part of the detector closest to the beam pipe. The main purpose of this subdetector

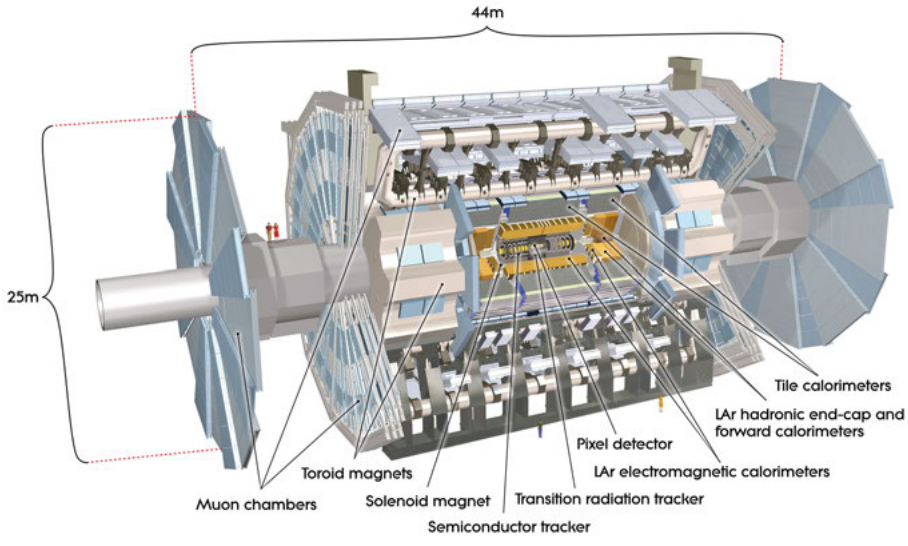

Figure 4.1. An illustrated overview of the ATLAS detector. [36]

is to provide high resolution measurements of the trajectories, "tracks", of charged particles. It is housed inside a solenoid magnet with a field strength of 2 T which curves the tracks of charged particles and the curvature of the track is proportional to the transverse momentum, p_{T}. The ID uses two detector technologies; silicon diodes in the Pixel and SemiConductor Tracker(SCT) detectors, and gaseous drift tubes in the Transition Radiation Tracker(TRT). Both technologies work on the principle that ionizing radiation traversing the sensitive material produce electrons that move in an applied electric field, the drifting charge then gives rise to a current that is measured. A hit is recorded using a time-over-threshold technique, i.e. if the current pulse is above a threshold for a certain time it is counted as a hit. The ID was designed to have an acceptance of $|\eta| < 2.5$ and a transverse momentum resolution $\sigma_{p_{\mathrm{T}}}/p_{\mathrm{T}} = 0.05\%$. The subdectors, as shown in figure 4.2, are placed with the pixels closest to he interaction point, followed by the SCT and the lastly the TRT.

4.1.1 The Pixel detector

The Pixel detector [37] is made up off rectangular modules with a sensitive area of 6.08×1.64 cm^2, and a thickness of 256 µm. The sensor is divided into segments, "pixels", 50 µm wide and 400 µm long.

In the barrel section the modules are oriented with the length of the pixels in along the z-axis and placed side by side on staves. The staves are

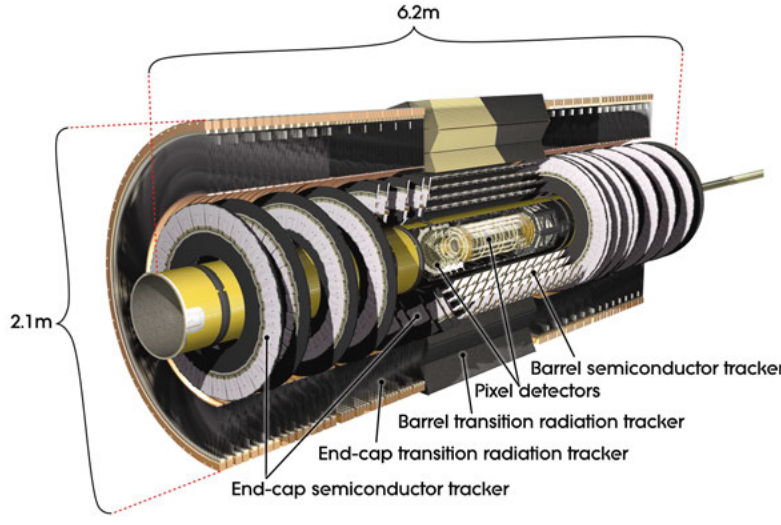

Figure 4.2. Illustration of the ATLAS inner detector.[38]

mounted to form three cylindrical layers at $r = 50.5$, 88.5 and 122.5 mm. The staves are tilted to allow the modules to overlap in the ϕ direction and compensate for the Lorentz angle, i.e. the drift of the ionization charges in the magnetic field. Before the start of run II in 2015, a fourth layer, the Insertable B-Layer(IBL) [39], was installed at the radius of 33 mm. This new layer has finer segmentation in z with a pixel size of 50×250 µm. In the endcap sections the modules are mounted on three disks with the length of the pixels in the radial direction.

4.1.2 The SemiConductor Tracker

The SCT has, similarly to the pixel detector, barrel layers and endcap disks of silicon diode sensors. However each silicon chip is only segmented in the ϕ direction forming so called "strips" with a separation of 80 µm and a length of 12 cm in the barrel sensors. In the endcap sensors the strips are not parallel but fan out radially with a pitch varying between 60 and 90 µm depending on the placement of the module. The lower resolution in z is compensated by using doublet modules, where each module has sensors on both sides rotated with an angle of $\pm$ 20 mrad with respect to each other.

4.1.3 The Transition Radiation Tracker

The TRT [40, 41] uses thin walled tubes or "straws", 4 mm in diameter, that are filled with a gas mixture and contain a central anode wire. In the barrel section the straws are parallel to the beam axis and closely packed between 56-108 cm in r for a total of over 50 thousand straws. The barrel straws are 1441 mm long and to reduce the occupancy the anode wire is isolated in the middle with readout channels for each section making the effective sensitive length shorter. In the endcap the straws are oriented radially and placed in wheels along z that are offset in ϕ to assure coverage in the transverse plane.

4.2 The calorimeters

The calorimeters are detectors designed to stop particles and measure the deposited energy. They are divided into two types; Electromagnetic (EM) calorimeters, which primarily stop electrons and photons, and hadronic calorimeters that stop hadrons. Muons can pass both types of calorimeters without stopping, but will be subject to multiple scattering i.e. they can loose energy and change direction through interaction with the material. Generally, each type is sensitive to both EM and hadronic showers[1] but the response and energy resolution can be tuned by the design and material choice. In ATLAS, hadronic showers often start in the EM calorimeter but continue in the hadronic calorimeter, while showers from e.g. photons and electrons are mostly contained within the EM calorimeter.

The ATLAS calorimeters are sampling calorimeters, i.e. they are made of alternating layers of sensitive material and stopping material. A sampling calorimeter will only measure a part of the deposited energy, the total energy of the incident particle is estimated from the sampled energy. The relative energy resolution for such a calorimeter typically takes the form

$$\frac{\sigma}{E} = \frac{a}{\sqrt{E}} \oplus b \oplus \frac{c}{E}, \tag{4.1}$$

where E is the energy of the incident particle, a is a stochastic term connected to the sampling and the shower development, b is a constant term due to detector construction imperfections and calibration errors, and c is a noise term which is mostly relevant at low energies. The calorimeters have an almost complete 4π solid angle coverage to facilitate the measurement of missing energy (see section 4.6.5).

[1] In fact, hadronic showers often include EM showers as part of the decay cascade process.

4.2.1 The EM calorimeters

The EM calorimeters uses lead as a stopping material and Liquid Argon(LAr) as the sensitive material. High energy electrons and photons that enter the calorimeter will loose energy through bremsstrahlung and pair production, initiating a EM shower of lower energy electrons and photons with a growing number of particles. As the energy of the shower particles decrease, more particles are stopped in the material and the shower dies out. The energy is measured from the ionization charges created as particles pass through the liquid argon, the charges are collected on electrodes interspersed in the liquid. Up to $|\eta| = 3.2$ the EM calorimeter has layers of lead and LAr folded into an accordion shape which assures coverage in ϕ, as shown in figure 4.3. The electrodes are segmented in three sampling layers in r and read out together with adjacent electrodes in $\eta \times \phi$. The layer closest to the interaction point has the finest granularity which helps separating showers from single photons and decays of hadrons such as $\pi^0 \to \gamma\gamma$. In addition to the three sampling layers, a pre-sampler consisting of a 1.1 (0.5) cm thick LAr layer in the barrel (endcap) is used to make a measurement of the particle energy before the showering. This measurement is used to correct the total measurement for energy lost in the absorber material. The energy resolution of the LAr EM calorimeter was measured with an electron test beam by fitting the result to equation 4.1. The fitted parameters were $a = 10\%\sqrt{GeV}$ and $b = 0.17\%$ for energies between 10-245 GeV [42].

In the region $3.1 < |\eta| < 4.9$ the EM Forward Calorimeter (EM-FCAL) consist of a copper absorber with cylindrical holes parallel to the beam line. The holes contain copper rods which act as read out electrodes and the gap between the rods and the absorber is filled with LAr. The granularity of this calorimeter is approximately 0.1×0.1 in $\eta \times \phi$. The resolution of this detector was also tested with a beam of electrons with the resulting parameters $a = 29\%\sqrt{GeV}$ and $b = 3.5\%$ [29].

4.2.2 The hadronic calorimeters

In the central region, up to $|\eta| = 1.6$, the hadronic calorimeter is constructed from tiles of steel absorber plates and a plastic scintillating material. Photomultiplier tubes are optically connected to the scintillators to measure the absorbed energy. The tiles are stacked in the z direction and several stacks with growing width form wedges approximately 0.1 radians wide, as seen in figure 4.4. 64 wedges of this type are used to cover the whole azimuth angle. The wedges are segmented in three radial layers and η so that the readout cells have a size of approximately $\Delta\phi \times \Delta\eta = 0.1 \times 0.1$ and 0.1×0.2 in the first and following layers respec-

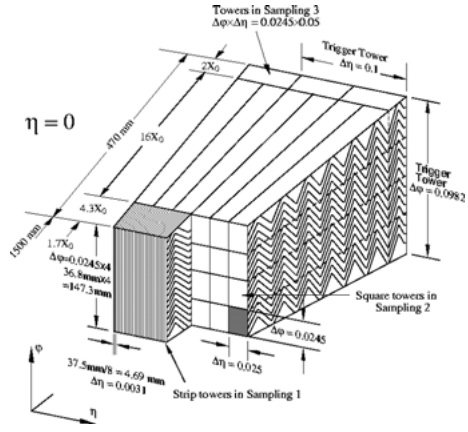

Figure 4.3. Details of a segment of the barrel LAr calorimeter. [29]

tively. The energy resolution of the tile calorimeter has been measured as $a = 56\%\sqrt{GeV}$ and $b = 5.5\%$ at $\eta = 0.35$ using a test beam of pions [29].

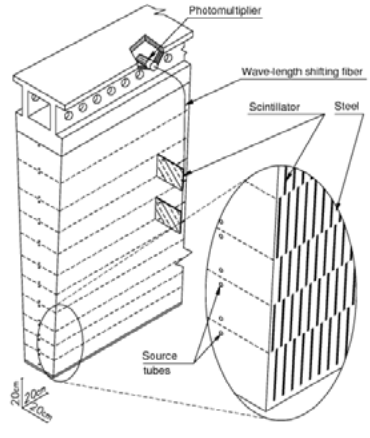

Figure 4.4. Schematic for a tile calorimeter wedge. [29]

In the high eta region, where the calorimeters must be more resilient to higher amount of radiation, LAr calorimeters are used. The Hadronic EndCap Calorimeter(HEC) covers the region $1.5 < |\eta| < 3.2$ and uses copper absorber plates orthogonal to the beam axis. In the region $3.1 < |\eta| < 4.9$ the hadronic forward calorimeter is very similar to the EM-FCAL but uses tungsten absorbers and rods. The resolutions for these two detectors were measured with pions and found the parameters $a = 71\%\sqrt{\text{GeV}}$,$b = 6\%$ for the HEC and $a = 70\%\sqrt{\text{GeV}}$, $b = 3\%$ for the hadronic forward calorimeter [29].

4.3 The Muon Spectrometer

The Muon Spectrometer(MS) surrounds the other subdetectors and is designed to make precise measurements and trigger on muons. It covers the region $|\eta| < 2.7$ and can trigger on muons with a pseudorapidity up to 2.4. The MS uses four different detector technologies; Monitored Drift Tubes(MDTs) and Cathode-Strip Chambers(CSCs) for precision p_{T} measurements, and Resistive Plate Chambers(RPCs) and Thin Gap Chambers(TGCs) for triggering and ϕ measurement. To measure the momentum of charged particles the parts of the MS are placed inside and around the toroidal magnets described in section 4.4. The barrel section of the MS is divided into 16 segments in ϕ, each with a set of precision and trigger detectors in three layers, as seen in figure 4.5. The sizes and radial positions of the detector modules alternate with the sections to create an overlap in ϕ. The endcap section consist of a set of wheels positioned to guarantee that a muon will pass at least three layers of precision measurement detectors for the whole pseudorapidity range. On each side of the detector there are two big wheels on the far side of the endcap toroid, i.e. away from the interaction point and a small wheel in front of the endcap toroid.

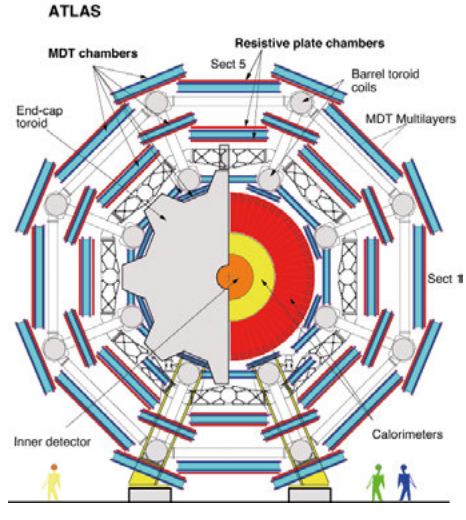

Figure 4.5. A schematic view of the muon spectrometer in the transverse plane of the barrel section. [29]

4.3.1 Monitored drift tubes

The MDTs are drift tubes with an Argon/CO_2 gas mixture, about 30 mm in diameter, with a central tungsten wire that collects the ionization

charge. The tubes are oriented along ϕ, to measure the track position in the bending plane, i.e r-z. Each layer has two groups of tubes stacked on top of each other (in the radial direction). In the innermost layers the groups contain four tubes while the outer two layers has groups of three. The relative resolution of the transverse momenta has been measured to be within the design value of $\Delta p_{\mathrm{T}}/p_{\mathrm{T}} \leq 10\%$ [43].

4.3.2 Cathode-strip chambers

In the high η region in the wheel closest to the interaction point the counting rate is too high to use MDTs, instead CSCs are used. These are multiwire proportional chambers, with anode wires between two cathode plates. The cathode plates on each side of the chamber have readout strips, one side perpendicular to the other so that a measurement of the track η and ϕ is made. The spatial resolution of the track hits is comparable to the MDTs so the use of CSCs does not degrade the resolution on p_{T} when combined with the outer MDT layers.

4.3.3 Resistive plate chambers

In the barrel section RPCs are used for triggering on muons and measuring the ϕ coordinate of tracks. The RPC have two resistive plates (about $10^{10}\Omega$ cm) with a 2 mm gap filled with a gas mixture. A high voltage system creates a uniform electric field between the plates. The RPCs are operated in avalanche mode, i.e. the voltage is set low enough so that the ionizing radiation creates an avalanche of electrons and positive ions that drift towards the anode and cathode plates, but the probability of creating a spark over the gap is less than 1%. This means that the RPCs can operate at very high rate and with a good timing resolution, which is desirable for triggering purposes. The RPC signals are readout by strips on the outer face of the resistive plates, with the strips orthogonal to each other on opposing sides. The RPCs are mounted together with the MDTs in the outer barrel layers, with four RPC chambers in the second and two chambers in the third layer. To minimize trigger signals from noise the chambers are used with a hit coincidence logic of three out of four for the second layer.

4.3.4 Thin gap chambers

In the endcap region the muon trigger and azimuthal coordinate measurement is done with multiwire proportional chambers with a thin gap between the wire and the cathodes. This thin gap makes it possible to

use a high electric field and short distances (1.8 mm) between the anode wires, which makes for a very good timing resolution. The anode wires are oriented to measure the radial coordinate of the track and one of the cathodes is segmented into readout strips orthogonal to the wires to measure ϕ. There are two layers of RPCs paired with MDTs in the small wheel in front of the endcap toroid, and seven layers on the big wheel closest to the endcap toroid. The seven layers on the big wheel are grouped in one triplet and two doublets. For muon triggering the triplet and doublets are used with a hit coincidence of two out of three for the triplet, and three out of four for the doublets.

4.4 The magnet system

The ATLAS detector uses superconducting magnets to provide magnetic fields that bend the trajectories of charged particles. The schematic layout of the magnet coils is shown in figure 4.6. A solenoid of length 5.8 m and radius of about 1.25 m provides an magnetic field for the inner detector. The field strength is 2 T at the center of the solenoid, i.e. along the beam axis. This field will bend charged particles in the η-ϕ plane. The high steel content of the tile calorimeter and the support structure acts as a return yoke for the solenoid. For the muon spectrometer, large toroidal magnets are used to produce magnetic fields with field lines parallel in ϕ, which will bend charged particle in the r-z plane. The eight barrel coils are 25.3 m long and have in inner and outer diameter of 9.4 and 20.1 m respectively. On each side there are also eight endcap coils, five meters long and with 1.65 and 10.7 m inner and outer diameters. The endcap coils are staggered in ϕ to fit between the barrel coils.

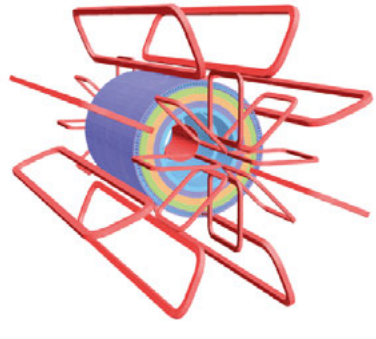

Figure 4.6. Schematic view of the ATLAS magnets (red), also pictured is the tile calorimeter witch steel and support structure acts as a return yoke. [29]

4.5 Trigger and data acquisition

The triggers are used to bring the event rate down to a manageable level, which is limited by the rate at which data can be offloaded to the CERN computer clusters for long term storage. Another factor is the sheer amount of data. At nominal luminosity and $\sqrt{s} = 8$ TeV a Higgs boson would be produced about every third second[2], while the peak bunch crossing rate is 40 MHz. Recording so many events and selecting potentially interesting ones offline[3] is not possible with the available computing resources or within a sensible time scale.

The triggers are divided into two categories; hardware triggers that use dedicated subdetectors and specialized processors, and software triggers that can use more detector information and run more complex trigger algorithms on conventional CPUs.

In run I, ATLAS used a three leveled trigger system; a hardware Level 1 (L1) trigger with a fixed maximum rate of 75 kHz, Level 2(L2) and the Event Filter (EF) software triggers with peak rates around of 6.5 kHz and 1kHz respectively [45]. The rates for the software triggers exceeded the design values, mainly due to higher than expected pile-up. The trigger and Data Acquisition (DAQ) system was restructured for run II. The L1 rate was increased to 100 kHz and the L2 and EF were combined into a High Level trigger(HLT) with an output rate of about 1kHz.

Data is first read out and buffered by Front End(FE) electronics, while data from the trigger detectors are piped to the L1 hardware processors. The L1 trigger makes a decision, within a latency of 2.5 µs, and sends it back to the FE. If an event passes the L1 trigger, the full detector data is read out from the FE buffers and stored in a second buffer accessible by the HLT trigger algorithms. The L1 trigger also defines Regions of Interest(RoI), i.e. a region in $\eta \times \phi$ around the trigger signal. The first HLT algorithms (L2 in run I) use the detector information inside the RoIs while subsequent algorithms can use the full detector information. The trigger and data acquisition flow for run II is shown in figure 4.7.

4.5.1 Hardware triggers

The ATLAS hardware triggers use information from the calorimeters and muon spectrometer(RPC and TGC hits). The triggers are designed to select events with objects relevant to the ATLAS physics programme, e.g high p_{T} muons, jets, electrons, photons, taus and large missing energy.

The L1 calorimeter triggers use low granularity trigger towers, combined calorimeter cells 0.1×0.1 wide in $\eta \times \phi$. For the L1 e, γ, τ triggers,

[2]Going by the total cross section measurement from [44].

[3]Here, "offline" is used in the sense that the processing happens after the data taking, on a system not directly connected to the detector.

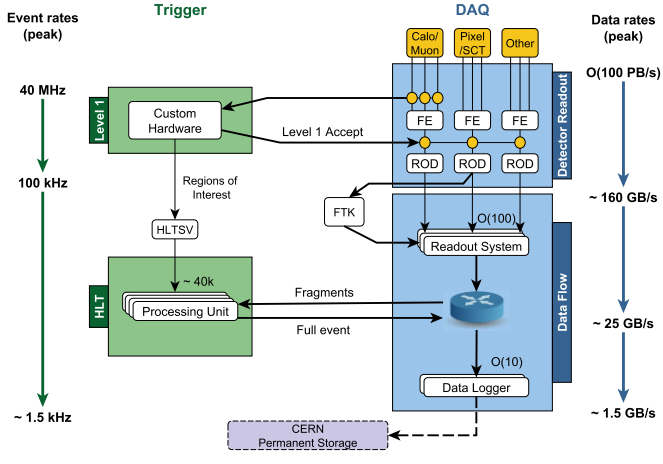

Figure 4.7. A diagram of the trigger and data acquisition flow during run II [45]. The L1 trigger runs at the LHC bunch crossing rate of 40 MHz and selects events to pass to the HLT. The L1 trigger generates an accept signal at a rate of about 1 kHz, which signals the DAQ to read out the full detector data from the front end buffers and propagate it to the HLT. The events are proceesed by the HLT where the final selection is made. The accept signal from the HLT signals the DAQ to send the data to long term storage.

16 of these trigger towers from the EM and hadronic calorimeters form a window with a 2×2 core (the RoI), as seen in figure 4.8. The trigger algorithm looks in overlapping windows so that any single tower will be included in 16 windows. The E_{T}[4] sum of each pair of the towers in the EM core is computed, and an L1 accept requires that at least one sum exceeds the trigger threshold. The e/γ triggers also require the sum of the surrounding towers in the EM calorimeter, and the sum of the hadronic calorimeter towers to be lower than some isolation thresholds. This is done to reduce false trigger accepts from jets. The τ trigger also require isolation in the EM and hadronic calorimeter, but excludes the 2×2 tower core of the hadronic calorimeter. The surrounding towers can be used for isolation requirements.

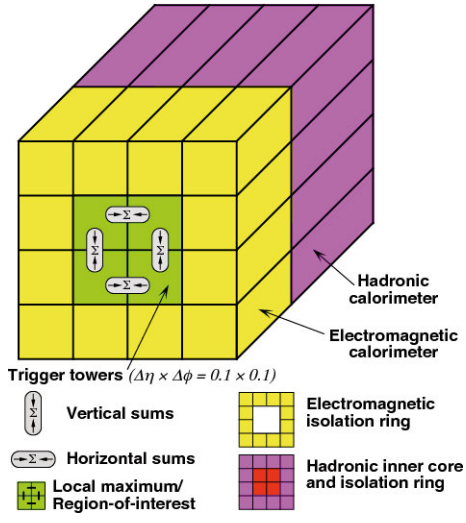

Figure 4.8. The L1 calorimeter trigger windows, made up of 16 low granularity trigger towers from the EM and hadronic calorimeters. [29]

The L1 jet triggers use windows of 16 or 32 towers and sum the E_{T} for the whole window in both the EM and hadronic calorimeter, which must be higher than the trigger threshold. The RoI coordinates is defined by the 2×2 tower region with local maximum E_{T} sum.

The L1 muon triggers look for hits in pivot planes, the second layer of RPCs in the barrel region and the last layer of TGCs in the endcap. The hits are linearly extrapolated to the interaction point and the trigger looks for hits in the remaining layers along the path. The p_{T} cut corresponds to the maximum deviation from this line. If matching hits are found, an RoI is formed from the η and ϕ measurements.

[4]The transverse energy $E_{\mathrm{T}} = E \cdot \sin(\theta)$.

The L1 calorimeter and muon triggers are combined in a Central Trigger Processor(CTP), which can issue L1 trigger accepts on for example multijet or dilepton events. The CTP also use the information from the other L1 triggers to compute the total and missing energy which can then be triggered on.

The efficiencies of the lepton triggers have been evaluated using a tag and probe method for $Z \to ll$ events in the following way. Events are required to have at least one lepton trigger object and two offline reconstructed leptons with invariant mass close to the Z mass. Since the event contains two leptons, one of them can be tagged while probing for a trigger signature matching the other. The efficiency is derived from the ratio of events with one or both offline leptons matched to a L1 trigger object. The electron and τ triggers reach efficiencies between 90-100% above certain p_{T} thresholds, while the muon trigger reach a plateau of about 70% in the barrel and 90% in the endcap. The larger muon inefficiencies stem from regions in the MS which are missing coverage due to the support structure.

Two additional triggers have recently been installed in ATLAS, the L1 topological trigger and a Fast TracK trigger(FTK), neither of which was available for the data used in Paper II or Paper III. The topological trigger is an addition to the CTP that can trigger on kinematical properties such as angular separation and invariant mass of the trigger objects. The FTK is the first hardware trigger in ATLAS to use information from the inner detector, but similar to the HLT it only considers data from the RoIs as defined by the L1 triggers. The FTK is a predecessor to the hardware track trigger foreseen for the high luminosity LHC which is discussed in detail in chapter 6.

4.5.2 Software triggers

The software triggers run on computing farms, with about 30000 CPU cores, located in a room close to the detector and connected to the data collection system with high speed optical links. In run I the HLT used two separate stages, an RoI seeded L2, and EF, on separate farms. The current HLT retains this approach but removes many of the bottlenecks by sharing CPU and memory resources. Tracking information from the ID is used to refine the selection made by the L1 calorimeter and muon triggers. In a first stage, hits from the Pixel and SCT inside an RoI are used to form low resolution track candidates by pattern matching. No track fit is made but the hits positions are compared to look up tables that store sets (patterns) of values corresponding to high p_{T} tracks. In the second stage the track candidates are extrapolated to the TRT and a track fit is made using the full granularity of the detector. For muons, the MDT are used

in a similar way to first produce track candidates that are then matched to ID track candidates for the final fit. Using tracking information for the lepton triggers yields a considerably better p_{T} resolution, and hence a steeper efficiency turn on curve rejecting many of the low p_{T} trigger signals from L1. The jet and missing energy triggers use reconstruction algorithms very close to those used for offline reconstruction, which will be discussed in the following section.

4.6 Reconstruction of physics objects

The raw event data that is recorded by ATLAS consist of the detector signals (i.e. the read out from the individual detector elements) and trigger decisions. This data is initially stored at the CERN Tier-0 computing facility. The Tier-0 is part of the Worldwide LHC computing Grid(WLCG) [46]. At this facility the raw data is also first processed into a format more suitable for physics analysis by reconstructing the data into events with physics objects such as leptons and jets. The raw and reconstructed data are distributed to Tier-1 facilities, large computing centers around the world, where they can be accessed for analysis. In this section the reconstruction methods for the objects most relevant for this thesis will be summarized.

4.6.1 Tracks and vertices

The hits in the Pixel and SCT detectors are grouped in clusters, i.e. contiguous pixels or strips that have been fired. The clusters are converted into space-points by converting the local coordinate on the silicon chip to global coordinates. In this step the two sides of the strip modules are used to get the z coordinate. The space-points are then fitted to helical track parameters using several methods including global χ^2 fits and Kalman filters as described in [47]. These methods take into account the scattering in materials in the ID and the non-uniformity of the magnetic field. The helical track parameters, visualized in figure 4.9, are:

- The transversal impact parameter, d_0.
- The longitudinal impact parameter, z_0.
- The azimuthal angle, ϕ_0.
- The polar angle, θ_0.
- q/p_{T}, the curvature which is inversely proportional to the radius.

The subscript 0 on the impact and angular parameters indicate that they take their values at the point of the closest approach to the z axis.

The reconstructed tracks are used to find both primary and secondary vertices [48]. A vertex is defined as the point in space from which particles originate, i.e. where the tracks converge. A primary vertex is the position

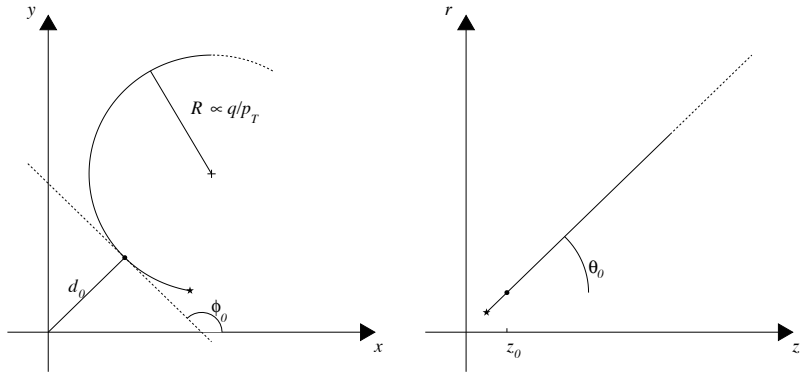

Figure 4.9. Illustration of the helical track parameters in the transverse (left) and longitudinal (right) plane. The coordinate system follows the description in section 4, with the origin at the interaction point and z along the beamline. A track is shown as a segment of a helix with the production vertex marked with a star.

of the scattering of partons in the pp collision, while a secondary vertex is the point of a decay. Many of the particles or resonances produced in a collision have lifetimes that are very short, and the secondary vertex in indistinguishable from the primary. However, some particles such as B-mesons can travel long enough for the difference to be noticeable. Vertex seeds are formed from the z_0 of the tracks and associated with a group of tracks. The tracks are then iteratively fitted to this vertex, removing tracks that have large χ^2 values after each fit. The primary vertices can be found by using a beam constraint on the fit, i.e. requiring that the vertex is not too far from the beam line. Secondary vertices, such as from b-jets or photon conversions, can be removed from the beam line by a significant distance and are found by an unconstrained fit.

4.6.2 Electrons

Electrons are reconstructed from clusters seeds in the EM calorimeter and a matching inner detector track [49]. The cluster seed is required to have a total deposited energy larger than 2.5 GeV. To discriminate against hadronic showers, the cluster must also have a large ratio of the energy deposited in the EM calorimeter compared to the hadronic calorimeter. Any cluster passing these requirements are used to look for a matching track in the ID. If no track is found, the cluster is considered for photon reconstruction. The energy measurement is taken from the deposited energy in the calorimeter while the η and ϕ coordinates are taken from the track. The energy is calibrated using scale factors and multivariate

techniques derived from MC simulations and validated with data. The reconstructed electrons might not correspond to a true prompt[5] electron; they can be "true fakes" real electrons e.g. from photon conversion or semileptonic hadron decays, and fake electrons from a combination of effects mimicking an electron, e.g. a muon that emits a hard bremstrahlung photon. To discern real prompt electrons from fakes ATLAS uses two methods, a cut based approach and a likelihood function. Both methods use input parameters such as the shower width, $\Delta\eta, \phi$ between the cluster and track, and ratio of the E_{T} and track p_{T} etc. The cut based approach simply places cuts on these variables, while the likelihood function uses the variable distributions for true electrons and fakes as probability density functions. Both methods define loose, medium, and tight selections which can be used to estimate the number of fake electrons in data using the matrix method [50]. The tight selection is typically used for the analyses, and is the case for the searches presented in this thesis.

4.6.3 Muons

Muons are reconstructed using tracks from the ID and the MS, and in some cases calorimeter information [51]. So called combined muons, start with a track fit of the hits in the MS, and muon candidates are selected based on a χ^2 cut. The track is then extrapolated to the ID and if a matching ID track is found, a new fit with hits from both the ID and the MS is done to reconstruct the muon track. If there are any unmatched tracks in the ID, i.e. not matched to any calorimeter clusters, they can be used to extrapolate out to the MS and to find muons that might have missing hits in the MS layers. If the ID track can't be matched to any track segments in the MS, the reconstruction algorithm searches the calorimeter along the tack extrapolation for signs of a minimum ionizing particle. If such signs are found the track is used to reconstruct a "calorimeter tagged" muon. The combined and calorimeter tagged muons can only be reconstructed within the acceptance of the ID, $|\eta| < 2.5$. Outside of this region stand alone muons can be reconstructed from the MS hits only. Sources for fake muons include semileptonic decays of hadrons, cosmic muons and punch through (particles from the calorimeter showers that travel all the way through to the MS without being stopped). The analyses in this thesis only uses combined muons as they have the lowest amount of fake muons and the best track parameter resolutions.

[5] A particle or track is said to be prompt if it originates from the hard scatter, and thus the primary vertex.

4.6.4 Jets

The jets used for the analyses presented in this thesis are reconstructed from topological calorimeter clusters [52] with the anti-k_{T} algorithm [53]. A topological cluster is formed by first finding calorimeter seed cells with a sufficiently high signal to noise ratio, where the noise can include both electronic noise and energy deposits from pile-up. Then the neighboring cells that have a signal to noise ratio above a slightly lower threshold are added to the cluster, if any cell neighbors two seeds the clusters are merged. This step is repeated until no more neighbors are added to the clusters. The deposited energy in the cells is measured at the EM scale, i.e. the energy is corrected using a calibration that maps the detector response to the energy of an electromagnetically interaction particle.

The anti-k_{T} algorithm takes the cluster four momenta as inputs,"pseudo-jets", and groups them together to form jets. The procedure compares each pseudo–jet and computes a compatibility of them coming from the same hard scatter, combining them if they are compatible within a resolution defined by a parameter D. The result is jets with a radius $\Delta R \lesssim D$. The advantage of this reconstruction technique over others is that it tends to produce nearly conical jets centered on the hardest pseudo-jet rather than merging many soft jets.

The four momentum of the resulting jets is calibrated to the jet energy scale(JES), which is derived from performing the reconstruction on truth particles and comparing to the jets from calorimeter clusters in simulation. This calibration is applied to jets in both data and simulation. For jets in data, another calibration is also used to account for differences in the simulated and real detector response. This calibration is derived from the jet measurement in events where the jet p_{T} can be balanced against an object that can be measured with good precision, such as $X \to Z + jets$ with $Z \to ll$. [54]

A jet is identified,"tagged", as originating from a b-quark using a multivariate technique; a neural network in run I and Boosted Decision Trees(BDT) in run II (see section 8.5 for a description of BDTs) [55]. The BDT is trained to separate b-jets from light and c-jets. Among the input variables for the BDT are jet p_{T} and η, and the properties of secondary vertices (e.g. the number of vertices, invariant mass of tracks, distance from the primary vertex etc.). In run II, Four efficiency operating points are defined by cuts on the BDT output score, $60, 70, 77$ and 85%. They are defined so that e.g 70% of all true b-jets in a testing sample have a score higher than the 70% working point cut. The rejection factor of c- and light-jets are 8 and 440 respectively.

4.6.5 Missing energy

The missing energy is calculated by its components in the transverse plane, i.e. E_x^{miss} and E_y^{miss} [56]. It is defined as the negative sum of the transverse energy for all calorimeter clusters matched to reconstructed objects ($e/\gamma, \tau$ or jets), topoclusters or tracks without a matching object, and muons:

$$E_{x,y}^{miss} = -E_{x,y}^{miss,calo} - E_{x,y}^{miss,muon} - E_{x,y}^{miss,unmatched} \tag{4.2}$$

The topoclusters that are not matched to any reconstructed object are included to account for low energy particles or particles outside of the inner detector acceptance. If such a cluster has a matching track, the energy contribution is taken from the track rather than the cluster as the tracks have better energy resolution at low p_{T}. Tracks with a good χ^2 are also included regardless if they have a matching cluster, this is done to account for low p_{T} particles that may not reach the calorimeters.

4.7 Detector simulation

A highly detailed simulation of the detector and its response to physical processes is very important for the ATLAS experiment. It is used to estimate the event yields and distributions of signal and background processes, the resolution of various parameters, and to evaluate new upgrades to the detector. The simulation is done using a framework called Athena [57] and can be divided into three main steps:

Event generation A physical process is generated by an event generator. This can be as simple as a single particle, e.g. a "particle gun", or the full generation of a proton–proton collision including a hard scatter, particle showering and underlying events. Anything more than single particles are generated using Monte Carlo(MC) event generators such as Pythia[58], Sherpa [59] and many more. The generation takes the theoretical description of the process (e.g. in the form a Lagrangian or Feynman diagrams) and produces events with the final state particles. At this point an event is simply a list of the final state particles and their four momenta. For a hadron collision the generation uses parton distribution functions (PDF) as well as the beam energy as input parameters. A PDF describe the density of gluons and quark flavors as functions of the parton longitudinal momentum and the interaction momentum transfer. Restrictions in our knowledge about QCD calculations mean that the PDFs can't be calculated directly but have to be derived from data. Several PDF sets have been produced with data from different experiments and the impact of the choice for our simulations

can be evaluated by comparing MC samples generated with the different sets, if the difference is large it is included as a systematical uncertainty. The particle showering is the process where quarks in the final state or gluons from radiation undergo the process of hadronization where new particles are radiated until the energy is so low that bound states form. The hadrons themselves are usually unstable but longlived enough that their decays are created in the detector simulation step.

Hit simulation The ATLAS detector is simulated with Geant4 [60] which uses a geometry model of the detector. This model specifies all the volumes, materials and magnetic fields. The Geant4 simulation take list of particles from the event generation and propagates them through the detector, hits are recorded from the energy deposition, timing and position. As the particles are propagated through the detector, interaction with the material (e.g. photon conversions, multiple scattering, etc) and decays and particle showers are also simulated. In addition to the hits, truth information such as the particle responsible for each hit, positions of decay vertices, and tracks are also stored.

Digitization After the hits have been recorded, the physical response of the detector is simulated. At this point several events can be merged, e.g. a hard scatter and minimum bias pile-up events. The hits are turned into "digits", i.e. a simulation of the digital signal from the detector read out systems. This step also simulates the electrical noise in the detector. At the end of the digitization, the simulated samples have the same format as the raw ATLAS data.

Reconstruction The reconstruction use the same code that reconstructs the data, using the procedures outlined in section 4.6, with the exception that truth information can be kept.

Typically, any ATLAS analysis needs large numbers of simulated events, at the order of several millions for both background and signal processes, to get a sufficiently small statistical uncertainty. The production of the simulated samples is done using the WLCG, but even with this large scale distribution the amount of physical processes that need to be simulated is to large. Therefore some processes use a simplified simulation, called AtlFast II (AFII), which speeds up the simulation by an order of magnitude [57]. In this simulation the particle showers in the calorimeters are not simulated with Geant4. Instead the particles that reach the calorimeters are used as input for parametrized shower shapes. The energy deposition in the calorimeter cells are then sampled from these shapes. The AFII and full simulation yield comparable results, with slightly lower resolutions for AFII. The validation of AFII use is generally done for each individual analysis.

5. The High-Luminosity LHC

The LHC will be upgraded to deliver a higher instantaneous luminosity, currently expected to start operation in 2026 [61]. The goal of the High Luminosity LHC(HL-LHC) is to deliver a total of 3000 fb^{-1} over ten years. To reach this goal, the instantaneous luminosity is expected to reach as high as 5-7.5 $\times 10^{34}$ $\text{cm}^{-2}\text{s}^{-1}$, which is 5-7 times higher than the nominal LHC luminosity. The number of pile-up interactions at this luminosity will be 140-200 per bunch crossing. The first upgrades to the accelerator will be done during the second long LHC shutdown (LS2) in 2019-2020, after which the luminosity will reach 2-3 times the nominal value. The final upgrades will be made during LS3 in 2024-2026, bringing the luminosity up to the aforementioned HL-LHC values.

The main contributions to the increased luminosity are a larger number of protons per bunch, a tighter squeeze of the β^*, and the use of crab cavities. Crab cavities turn the bunches, which are shaped as oblong ellipsoids, so that they cross each other sideways, thus increasing the effective area of the bunch crossing.

5.1 ATLAS detector upgrades

The motivation for the HL-LHC upgrade is to increase the number of events that are of interest for the experiments. Precision measurements of processes including the SM Higgs boson are of special interest. Searches for BSM physics and rare processes will also benefit from the large amount of data. Naturally, the background rates will also increase and to take advantage of the higher luminosity the experiments must improve their trigger capabilities. One of the main obstacles is the large amount of pile-up interactions which will increase the occupancy in the whole detector. The ATLAS detector will be upgraded for the HL-LHC in two phases, Phase-I [62] and Phase-II [63] during LS2 and LS3 respectively. These upgrades will see substantial changes to many of the subdetectors and TDAQ systems, in the following sections only the changes most pertinent to the development of a hardware track trigger will be summarized.

5.1.1 Phase-I upgrades

The Phase-I upgrade [62] includes a New Small Wheel(NSW) in the MS, replacing the current small wheel with new trigger and precision detectors. The new trigger chambers are an updated version of the TGC with

finer granularity strips. A large contribution for fake muons in the L1 muon triggers in run I was charged tracks that doesn't originate from the interaction point but travel through the endcap toroid, and later the trigger chambers in the big wheel. For run II the requirement of a hit in the TGC in the small wheel reduced the fake rate substantially. With the improved resolution for the NSW the rate is expected to be reduced even further.

The calorimeters read out systems will also be upgraded for Phase-I. The trigger towers will receive a finer granularity to deal with the occupancy and better distinguish between photons, leptons and jets.

5.1.2 Phase-II upgrades

The details of the Phase-II upgrade are still under development. The initial plans were presented in the Letter of Intent(LoI) [63] and the latest designs are discussed based on different costing scenarios in [64]. One of the major changes to the detector in Phase-II is the replacement of the ID. The current ID was only designed to withstand the radiation up to run III, and would not survive the HL-LHC era. The new ID must be able to handle the high occupancy, the SCT and TRT of the current ID would be highly saturated with a pile-up of 200. Therefore, the design for the new ID, the Inner Tracker(ITK), uses only pixel detectors and strip sensors with a finer granularity. The main design from the LoI, used in many of the studies for the hardware track trigger described in chapter 6, is shown in figure 5.1. In this design the two innermost pixel layers in the barrel use pixels of size $25\times150\,\mu m$, the outermost layers and the endcap disks use pixels of size $50\times250\,\mu m$. The strip sensors have a pitch of $75\,\mu m$ and either short (≈ 24 mm) or long (≈ 48 mm) strips. The three inner barrel layers use short strips, while the rest use the long strips.

Other proposals for the ITK layout, to be considered as the new baseline, includes using five pixel layers and four strip layers in the barrel region and inclined pixel sensors. Using inclined sensors will reduce the cluster size as tracks at high η pass the sensors in a more perpendicular fashion, while diminishing the total active area of the sensors and thus reducing the cost. Performance studies using these layouts have been presented in [65].

The trigger architecture of ATLAS will also be revised for the Phase-II upgrade. The HLT computing farms and the data transfer systems will be replaced with new hardware, and is expected to be able to handle an output rate of 5-10 kHz. The baseline for the hardware triggers has been to use a two level trigger, with a L0 similar to the Phase-I L1 triggers with an output rate of 1 MHz, and a L1 trigger with an output rate between $200-400$ kHz. More recently, the baseline has shifted to using

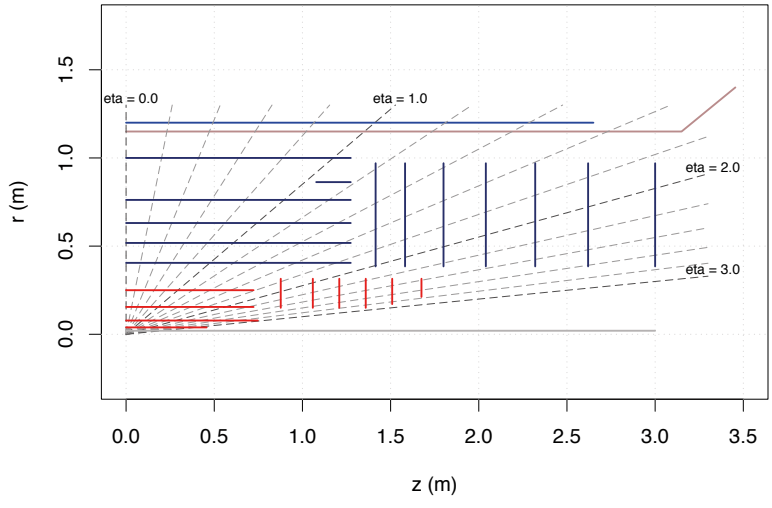

Figure 5.1. The ITK design from the Phase-II letter of intent [63] with the pixel layers in red and the strip layers in dark blue. The blue line near $r = 1.2$ m marks the position of the solenoid magnet.

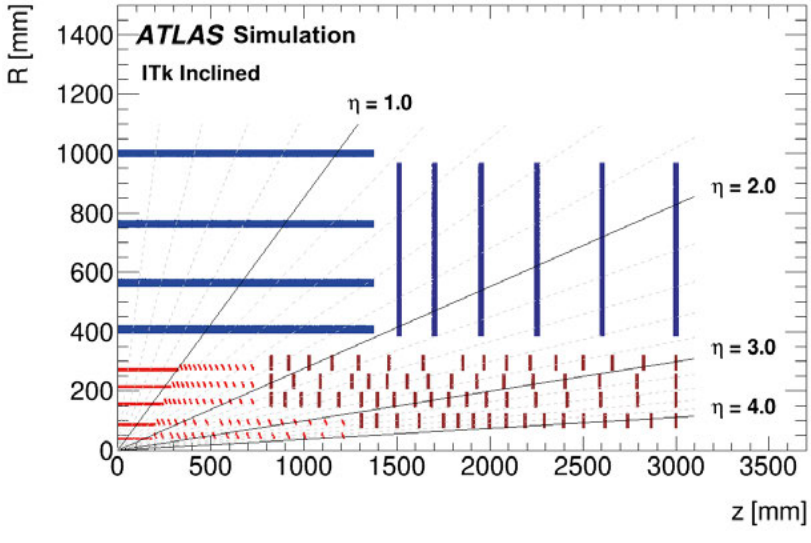

Figure 5.2. An alternative ITK design from [65], with the pixel layers in red and the strip layers in dark blue. This layout features inclined pixel sensors.

a single L1 trigger operating at 1 MHz. This option requires the use of MDT for the muon trigger, which current read out systems only support a read out rate of about 200 kHz. To use the MDT at L1 all the read out electronics must be replaced, which is a costly operation. Therefore, the TDAQ system is being developed to accommodate both versions. A key requirement to achieve the physics goals of ATLAS is to have a high efficiency trigger for low p_{T} leptons, i.e. around 20 GeV. Even with the L1 calorimeter and muon trigger upgrades from Phase-I, the rates at the HL-LHC would be too high at a trigger threshold of 20 GeV. The next chapter describes the studies of using track information for this purpose. The L0/L1 trigger option will include a hardware track trigger (L1Track), seeded by the L0 RoIs providing tracks to the new L1Global which makes a final L1 accept decision based on the tracks and the other L0 triggers. In the single level option, a hardware track trigger can be used at the level of the HLT for regional tracking.

6. Hardware track trigger design

Using track information increases the p_{T}, η and ϕ resolutions of trigger objects. Requiring that a calorimeter cluster or a MS track have a corresponding track in the inner detector can also reduce the number of fake triggers and improve particle identification. Using the track information as early as possible in the trigger chain is therefore always desirable, and a necessity to keep the rates low enough at the HL-LHC. Performing track fits is a time costly operation as the number of hit combinations is large, and usually includes some way of limiting the number of hits considered for each track. In ATLAS the baseline strategy is to use an RoI seeded approach, where only hits from a small volume ($\approx 10\%$) of the detector are considered. Another approach is to use a self-seeded trigger, where the detector modules in a single layer provide small track seeds of 2-3 hits. These track seeds are extrapolated to the other layers and nearby hits can then be propagated to the track fit. Such an approach requires specialized sensors and read out electronics and is not in line with the ATLAS upgrade plans, but is considered for the CMS experiment [66].

To increase the number of hits further, a pattern matching method can be used. A pattern consist of coarse resolution hits, one per detector layer, and is constructed from the simulation of single particle events. The resolution of the patterns are defined by the superstrip size, e.g. how many strips and/or pixels that result in the same coarse resolution hit. Figure 6.1 illustrates a track and its pattern of superstrips. The ITK strip modules in the barrel all have 1280 strips each, a superstrip width of 10 would then mean that the module has 128 superstrips. The name superstrip is used for the pixel layers as well, where a superstrip length is also defined for the number of pixels in z. Patterns are generated for the desired acceptance range of the track parameters and stored. Before running a track fit on the hits in an RoI, all hits are first compared to the stored patterns. A pattern can be considered matched if it has matching hits in all or a subset of the layers. All hits that doesn't lie within any matched pattern are then discarded, while the rest are propagated to the track fit.

In ATLAS this method is already in use for the HLT and offline tracking, but has also been developed for a hardware trigger, the FTK [67] which will be part of the trigger chain from run II up until the HL-LHC. The FTK has been designed to use the current L1 calorimeter and muon triggers for the RoI seeding and provide tracks within a latency of 100 µs

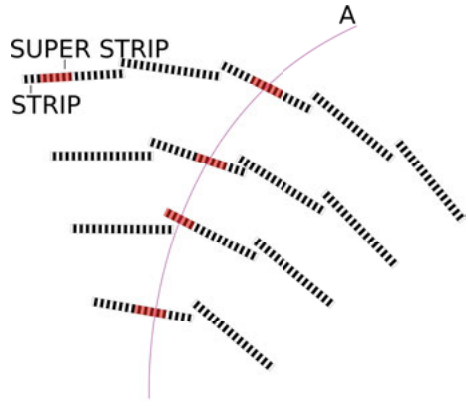

Figure 6.1. A pattern is formed by identifying the superstrip hits (red) from a simulated track (purple).

at a pile-up of $\mu = 60$-80. The main difference for the hardware track trigger at the HL-LHC (the L1Track) is that it has to cope with pile-up up to $\mu = 200$ and have a latency of $\approx 30\,\mu s$. The L1Track follows the FTK design of using Associative Memory(AM) chips to do the pattern matching and FPGAs to do the track fitting.

Paper I describes the simulated performance of a L1 track trigger, using the LoI ITK layout. The following sections will give some background information on the methods used to achieve those results. The last section of this chapter concerns a general comparison of an AM based pattern matching and using the Hough transform to filter the hits for the track fitting stage. This comparison is the basis for Paper IV.

6.1 Pattern matching with associative memory chips

The AM chips are very-large-scale integration(VLSI) circuits developed to store patterns and perform the pattern matching in a parallel fashion. A description of the construction and use of these type of chips for the FTK can be found in e.g. [68]. A schematic description of the AM chip is shown in figure 6.2. Prior to the pattern matching, all hits in the RoI are first formatted to find the corresponding superstrip ID (SSID). This ID is a hit word (16 bits long for the FTK) constructed from the unique module number and the superstrip position local to the module. The full resolution hits are stored in the Data Organizer(DO), a database with the superstrip ID as the look-up key. The patterns are stored in the AM chip with each layer superstrip ID in a node. Each node is connected to a bus for the hit word to be compared and a matching flip-flop. The node compares the hit word to the stored memory content, i.e. the pattern

superstrip ID for that layer. If it is a match, the flip-flop output is set to high (i.e '1'), otherwise it retains its old value. The flip-flops for a pattern is connected to a majority counter. If the sum is greater than the number of layers needed for a match, the address of that pattern is sent to the DO. The DO then reads the pattern superstrip IDs and sends the corresponding full resolution hits to the input for the track fit.

The current AM chips for the FTK can store around $130 \cdot 10^3$ patterns. New chips are being developed for the Phase-II track trigger [69] and are expected to be able to store around $500 \cdot 10^3$ patterns.

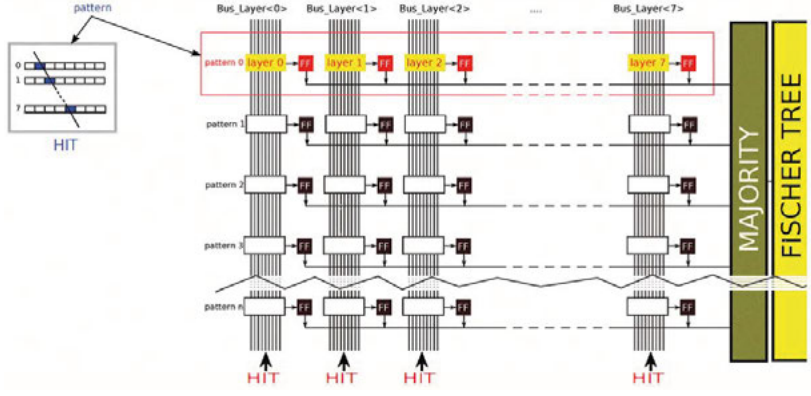

Figure 6.2. A schematic diagram for the AM chip pattern matching. [67]

6.2 Track fitting

The track fitting is done in FPGAs where the estimations for the track parameters ($\bar{p}_i$) are extracted from the hit positions:

$$\bar{p}_i = \sum_{j=0}^{N} C_{ij} x_j + q_i, \tag{6.1}$$

where x_j is the hit position in layer j, and C_{ij} and q_i are fit constants. The constants are precomputed from single particle simulation hits using principal component analysis. This is a linear approximation of the track parameters and is only valid in continuous regions of the detector, e.g. it's not valid over multiple modules which overlap in ϕ. Therefore the constants are stored by sectors, with each sector being a combination of one module from each layer. The χ^2 value of the fit can be retrieved in a similar way with another set of constants.

6.3 Design of the L1Track trigger

The requirements of a L1 track trigger for the HL-LHC was defined in the Phase-II letter of intent [63]. The main purpose is to provide high quality tracks for the L1 global and HLT triggers within a short latency, i.e. about 30 µs and reducing the background trigger rates. Since the luminosity increases with about a factor five, the target rejection factor of background events is also five. This has to be done while keeping a good efficiency, at least 95% for leptons, with respect to the offline reconstruction.

6.3.1 Latency

The latency is split between the readout of the ITK, AM pattern matching and track fitting. The ITK might not be read out in full for the L1 triggers, as this would require a huge bandwidth at a 1 MHz L0 accept rate. Instead, about 10% of the ITK will be read out via regional readout requests(R3) defined by the L0 calorimeter and muon RoI. Each event usually contains several RoIs, especially at high pile-up conditions. A conical RoI size of 0.2×0.2 as defined by a cluster in the calorimeter will cover about 0.1% of the tracking volume. However, the beamspot of the HL-LHC can have spread up to ± 150 mm from the center. Thus to have a chance of finding the track responsible for the cluster, the RoI must be wedge shaped covering this region, this means an RoI of 0.2×0.2 will include about 1% of the ITK volume.

The R3 data is also limited in size and will only include the clusters of width smaller than four strips/pixels. The time it takes to transfer the R3 data depends on the occupancy of the region but also the number of readout chips per sensor and their bandwidth. The largest latency is expected from the strip modules in the middle of the endcap disks as they are located in a "perfect storm". They are in the high η regions where the occupancy is higher, the geometry requires them to have a large number of strips per readout chip, and the bandwidth for the strip system is lower than for the pixel detector. The pixel layers have a higher occupancy than the strip layers as they are closer to the interaction point, however the pixel detector was designed for full readout at 500 kHz, and only the innermost barrel layers are expected to have latencies incompatible with an R3 readout. Therefore the L1Track studies have focused on using one or two of the outermost pixel layers in the pattern banks. The R3 requests will compete with full readout requests from the L1Global accept, to ensure that the latency for the track trigger doesn't become too long the R3 requests are given a priority. With this priority in place, it has been shown that the 99% of all R3 requests can be completed within a latency of 6 µs [70].

The pattern matching can start as soon as the first R3 data has been formatted in the DO, and the latency of the matching is dependent on the clock speed of the AM chip and the number of clusters to process. One SSID can be loaded onto the AM chip for each clock cycle, e.g. with a chip running at 200 MHz and 200 clusters in the layer with most occupancy the latency is 1 µs. After this time the patterns can be read out and sent to the fitter, at a rate of 200 MHz.

A track fit can start as soon as a pattern has been readout from the AM chip. Compared to the pattern matching, the latency of the track fit is not linear with the number of hits since it will have to perform one fit for each combination. With an FPGA that is able to perform a track fit in 0.25 ns the combined latency of the pattern matching step and track fitting would be a few µs if the number of patterns (track fits) are at the order of 100 (1000).

6.3.2 Definition of the regions

Comparing the hits in the R3 data to all the patterns for the whole detector is unnecessary, the RoI coordinates can be used to send the data to pattern banks trained on smaller regions. In our studies these regions are similar in size to the RoIs, but they are defined by the track parameters of the muons rather than hit positions in the detector. Due to the azimuthal symmetry we always use the same region in ϕ (for the design studies), the muons are generated with $0.3 \leq \phi \leq 0.5$. The region is varied in η but also there with a size of 0.2. To ensure that tracks aren't missed at the boundaries of these regions, they would overlap in both ϕ and η. Depending on the amount of overlap, the number of regions for triggering up to $|\eta| < 2.5$ is $\mathcal{O}(1000)$. The FTK use about one billion patterns for the full detector, using this as a baseline the target pattern bank size for L1Track is one million patterns per 0.2×0.2region. The number of patterns can not be increased too much as it is one of the main factors in the cost of the system with one AM chip/500k patterns.

6.3.3 Pattern matching efficiency

The LoI layout of the ITK has four pixel layers and 5 layers of strip doublets in the barrel region. In the pattern matching the strip doublets are counted as separate layers and this layout would have 14 logical layers. Using all the layers have several drawbacks; More data must be transferred and the number of patterns per region grows as there are more possible combinations. Using to few layers also introduce problems; The resolution of track parameters in the fits is degraded, and the efficiency is lower since a track might be missing a hit in one of the layers. A com-

promise was found by using eight logical layers and a 7/8 hit requirement for matching.

An efficiency above 90% for leptons can be achieved quite simply by generating patterns with a large number of training events, e.g. $\mathcal{O}(30 \cdot 10^6)$ per region in our studies. However this usually results in large pattern banks with several million patterns. Using a larger superstrip width will decrease the amount of patterns without loosing efficiency, in fact it gets better if the number of training muons is low. Using larger superstrips increase the risk of spurious hits, e.g. from different low p_{T} tracks or noise, to mimic a high p_{T} track. This reduces the hit rejection from the pattern matching and relies on the track fitter to resolve those "fake patterns". Each extra hit propagated to the track fitter can result in many more fits, as it has to try all the combinations of hits in the different layers. Thus, to keep the number of fits, and thus the latency, low it is much more economic to reject as many hits in the pattern matching step as possible.

By using don't care(DC) bits, the superstrip width can be varied on a pattern-by-pattern and layer-by-layer basis. A don't care bit is a "ternary bit" that can take the values '0','1' or 'X' (don't care). In hardware a ternary bit is using two ordinary bits, so for 16 bit hit word the pattern in the AM chip has to use 18 bits for two DC bits. If the least significant bit of the hit word, i.e. the bit separating a superstrip from its immediate neighbor, is set to don't care the superstrip width is effectively doubled. Using a DC bit for the next bit as well, the superstrip width is doubled again. This method significantly reduces the number of patterns by combining patterns that only differ by a few superstrips in some layers. Since most patterns and layers retain the nominal superstrip width, the number of matches from spurious hits are not increased to the same degree as just using a larger superstrip width. An illustration of patterns with DC bits and wildcards is shown in figure 6.3.

Even when using DC bits, the pattern banks can grow larger than our nominal 1 million. Since we train on around 30 million muons and get pattern banks at the order of a few million, it stands to reason that some muons produce the same patterns and some might be more common than others. Therefore, as a last step the patterns are sorted by their usage count, i.e. the number of training muons that generated that exact pattern. Then, as the bank is used for pattern matching only the first million patterns are used. Truncating the pattern bank in this way showed very little impact on the efficiency.

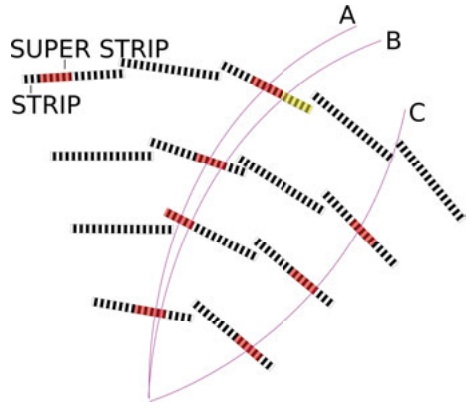

Figure 6.3. Illustration of the pattern generation. Track A and B only differ by one superstrip in the last layer and can be combined with a don't care bit. Track C is missing a single hit and can use a wildcard for the last layer.

6.3.4 Simulation of the pattern matching and track fitting

The inputs for the simulation are single lepton and minimum bias events with a pile-up of 200. These samples have been produced using the ATLAS simulation framework as described in section 4.7. Samples with single muons are used for the pattern generation, electrons and taus could in principle be used to train alternative sets of patterns, but so far the muon pattern banks have proven to be efficient at matching electron and pion tracks as well. Pattern matching and track fitting are evaluated using the single lepton samples, the minimum bias samples or a combination of the two (i.e. overlaying a single lepton event with a minimum bias event). In addition, samples of di-jet and leptonically decaying b-jets which are large sources of fake lepton triggers for the current L1 electron and muon triggers, have been used to evaluate the rejection of those backgrounds.

The pattern generation, matching and track fitting are run using a framework standalone from the ATLAS simulation. Generation of the patterns is done by first specifying the logical layers to use, how many wildcards are allowed and the superstrip sizes (which can be different for the different layers). The code then loops over the single muon events for a given region. For each event, the clusters with a width < 4 that come from the primary particle are used to build a pattern. The hit positions in the logical layers are formatted to superstrips. If a pattern has more missing layers than the allowed wildcards, the event is discarded. Otherwise it is compared to a set with all patterns found so far, and if an identical pattern exists it's usage count is incremented. After the code has run over the full set of events, the patterns are compared to each other and combined into DC patterns if possible. When patterns are combined

with DC bits their usage count is also added. After all patterns have been compared, the new set of patterns are sorted by the usage count and stored.

Similarly, the fit constants are generated from single muon events where first all the needed sectors are defined from the tracks. Then the fit constants for the parameters and the χ^2 are computed for all the sectors, averaging over all the training muons using a specific sector. A usage count for the sectors can also be defined at this stage, the impact on fitting efficiency and latency is under investigation.

When running the pattern matching the pattern bank is loaded sequentially starting with the highest usage count until it has loaded all the patterns or until it reaches a limit, usually set to one million patterns. Simulation of the pattern matching as it is done in the AM chips is not efficient on a CPU as each hit must be compared to every pattern one at a time. Instead all the superstrip IDs of the used in the pattern bank are stored as elements in a map, the patterns then contain pointers to these elements. This means each hit to only be compared once. A pseudo code for the pattern matching is shown below.

```
Load in patterns from pattern bank;
Load in fit constants mapped to cluster positions;

for (pattern in pattern bank)
  for (number of logical layers)
    Insert the SSID in the SSID map;
    Set the patterns pointer for this layer
    to point to the map element;

for (event in sample)
  for (clusters)
    if (cluster width < 4)
      Construct SSID from cluster;
      Find SSID in map;
      if (found)
        Set SSID fired at this event number;
        Add the full resolution hits
        to the patterns cache (clear first if
        it's a new event);

  for (patterns)
    Count the number of SSID fired at this event;
    if (count > 7)
      Nmatch += 1;
```

```
      Note the pattern index to send to fitting;

  for (matched patterns)
    find the fit constants for the full resolution
    hits from the matched pattern and compute track
    parameters;
```

6.3.5 Results of the track trigger studies

The results presented in Paper I show that a L1 hardware track trigger is a viable option for ATLAS in the HL-LHC era. The trigger is able to provide tracks with good quality, especially when using information from the pixel detector. The resolution of the track parameters for single muons are comparable to those of the FTK and offline tracking [67]. The background rejection of the track trigger was tested with samples of events expected to pass the seeding lepton triggers (i.e. L0, or the current L1). For this test, both the background and single muon samples were overlaid with a pile-up of 200 minimum bias events. By using simple cuts on the track p_{T} and quality, e.g. χ^2, is was possible to reduce the amount of background events passing the L1 track trigger by a factor ≈ 5 while keeping the efficiency for single muon events high. This is a promising result, however, further studies are needed to evaluate the performance of the trigger using benchmark signals (e.g. SM or SUSY particle decays with leptonic final states) and a full simulation of the seeding trigger.

In Paper IV, the pattern matching method was compared to a hit filtering based on the Hough transform, which has also been investigated for the ATLAS [71] L1Track trigger. The two methods were tested using a generic tracking detector simulation and it was found that while both methods did provide a substantial rejection of hits, the pattern matching generally performed better.

While the results in Paper I were produced using the ITK layout from the Phase-II LoI, similar results have been achieved using the newer layouts. The main change of the new layouts compared to that of the LoI was the addition of a pixel layer and the removal of a strip doublet layer. As the L1 track trigger only use a subset of the layers, this had little impact on the performance. The only difference being that the patterns and fit constants have to be reproduced with a new selection of layers. For the pattern matching, the inclined layout did not pose any problems as the hit positions are mapped to logical layers which do not care about the orientation of the sensors. As the ITK layout and the TDAQ structure for the upgrade continues to evolve, the final design of the track trigger will also change and be adapted accordingly.

Part III:
Charged Higgs boson searches

7. Previous searches

There have been many searches, both direct and indirect, for charged Higgs bosons in previous experiments as well as at the LHC, the ones most related to this thesis are summarized below. No evidence for a new boson has been observed so far and large parts of the parameter space of the 2HDMs have been excluded. Most searches have focused on light charged Higgs bosons but with the higher collision energy of the LHC the high mass range is now also being probed.

The combination of searches by the four LEP experiments, summarized in [72], could exclude charged Higgs bosons with masses lower than 80 GeV and 72.5 GeV for a type II and type I (with $m_A > 12$ GeV) 2HDM respectively. These searches looked for pair-produced charged Higgs bosons through a Z with the H^+ decaying to either $c\bar{s}$, $\tau\nu$ or W^*A.

At the Tevatron $p\bar{p}$ collider the CDF experiment searched for a light charged Higgs decaying to $c\bar{s}$, and D0 searched for $H^+ \to tb$ in the mass range 180 to 300 GeV. The tb search put upper limits on the production cross section times branching ratio between 14-5 pb for $\tan(\beta) \geq 1$ in a type II 2HDM. In addition to these direct searches both experiments were also able to put upper limits on the $t \to H^+b$ branching ratio by comparing $t\bar{t}$ branching ratios to the SM predictions [73].

ATLAS and CMS have published searches with the $c\bar{s}$ [74, 75], $W^{\pm}Z$ [76], $\tau\nu$ and tb final states [77, 78, 79]. The $\tau\nu$ searches have excluded most of the allowed space on the $m_{H^+} - \tan(\beta)$ plane for light charged Higgs bosons, as shown in figure 7.1. The remaining allowed region is hard to exclude due to the fact that the production cross section has a minimum around $\tan(\beta) = 7$ and a lower branching ratio when the H^+ mass is close to that of the top quark. For a heavy H^+ the $\tau\nu$ searches are less sensitive and exclude a smaller portion in the high $\tan(\beta)$ region as shown in figure 7.2. The CMS search for $H^+ \to tb$ looked for the single lepton, dilepton[1] and $\mu\tau_h$ final states. Limits where extracted by comparing the distributions of b-jet multiplicity and H_T, the scalar sum of p_{T} from jets pointing to the primary vertex, to the expected SM yields, assuming a branching ratio of one for $H^+ \to tb$. The combined limits for the three final states ranged from 1.99 pb to 0.13 pb for $m_H^+ = 180$ to 600 GeV. The

[1]Due to the considerably different detector signature and reconstruction for τ-leptons, it is customary to treat them as a separate category. Hence "dilepton" refers here to a combination of electrons and muons.

searches in the $W^{\pm}Z$ final state are interpreted in the Georgi-Machacek (GM) model[80] which includes a Higgs-doublet and a triplet. This model allow a $H^{+} \rightarrow W^{+}Z$ decay at tree level as opposed to 2HDM where it is only allowed at the loop level.

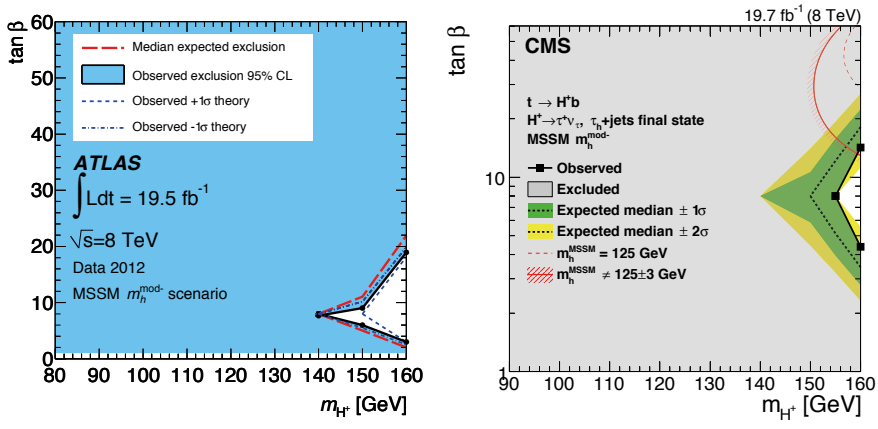

Figure 7.1. Excluded regions in the $m_{H^+}/\tan(\beta)$ plane for the m_H^{mod-} scenario by ATLAS [77] and CMS [79] searches.

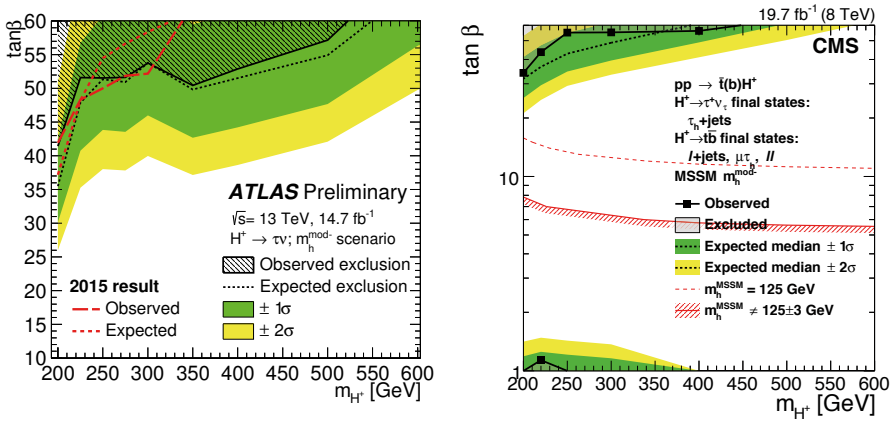

Figure 7.2. Excluded regions in the $m_{H^+}/\tan(\beta)$ plane for the m_H^{mod-} scenario by ATLAS [78] and CMS [79] searches.

Results from precision measurements on SM processes have also been used to constrain the parameter space of the charged Higgs boson, such as b-hadron decays where the H^{+} would interfere with the processes including a W. An interpretation of results from the BABAR experiment was done by [81] and concluded that most of the results were only compatible with a $\tan(\beta) < 20$ and m_{H+} larger than 380 GeV, and the measurement

of the branching ratio for $B \to D^* \tau \nu$ is only compatible with low masses and high $\tan(\beta)$. Thus this seem to suggest that the type II 2HDM is a weak candidate for BSM physics, however it is still used for as a benchmark scenario for direct searches as other BSM processes might interfere with these measurements. Furthermore, new results have relaxed the limits from $B \to D^* \tau \nu$ suggesting that a charged Higgs boson might be allowed for masses larger than 600 GeV and $\tan\beta > 1$ [82] in a Type II or III 2HDM.

8. $H^+ \to tb$ searches with ATLAS

The branching ratio, $BR(H^+ \to tb)$, is generally the dominant one for charged Higgs boson masses above the top quark mass, i.e $m_{H^+} \geq 173$ GeV. This thesis is based on two searches in this channel performed by ATLAS, presented in Paper II and Paper III. The first sections in this chapter present some common features of both analyses and are then followed by some discussion on the details each analysis. In addition, the use of the dilepton final state is discussed.

8.1 Signal & background features

The dominant production mode of a heavy charged Higgs boson in a pp collision is through a tb vertex, which means it will be produced in association with a top quark, shown in figure 8.1. Each of the W bosons from the two top quarks can decay either hadronically into two light jets or leptonically into a lepton and a neutrino. Thus the final state will include four b-jets and either four light jets, two light jets and a lepton or two leptons. The fully hadronic final state has the largest branching ratio but, due to large QCD backgrounds at the LHC, the possibility of triggering on a lepton makes the single and dilepton final states better candidates for a search. The single lepton final state has again the largest branching ratio and was the sole channel used for the search for Paper II and Paper III. The dilepton final state offers a "cleaner" signature with less jet-activity and is thus less sensitive to missidentified leptons. The main benefit of including the dilepton channel is for searches in the lower mass region (below 500 GeV or so), the signal over square-root of the background for a combined search is of the order of 10-20% better in this region than for the single lepton channel only. The main background comes from $t\bar{t}$ pairs, with possible additional heavy flavor initial state radiation shown in figure 8.2. In following sections this background is divided into the groups $t\bar{t}$+light with no or light jet radiation, $t\bar{t}+c$ and $t\bar{t}+b$ with at least one charm or bottom quark. The two last categories are collectively referred to as $t\bar{t}$+HF (Heavy Flavor). Other, smaller, backgrounds include top pairs produced in association with a vector boson($t\bar{t}V$) or the SM Higgs boson($t\bar{t}H$), W or Z + jets, single top and diboson events.

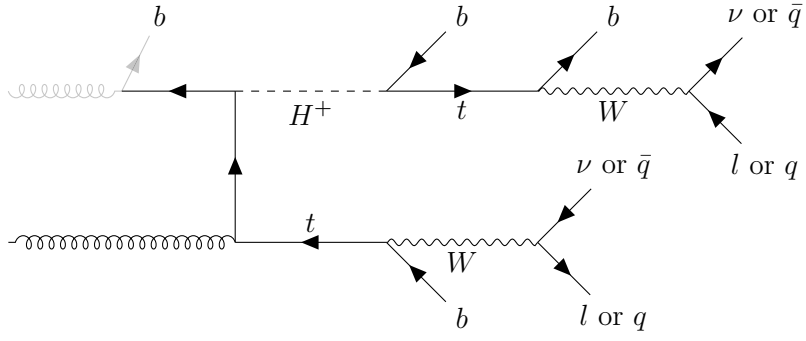

Figure 8.1. Feynman diagram of the $H^+ \to tb$ decay, the gray part shows the 4FS process where the inital b-quark is produced in gluon splitting adding another b-jet to the final state.

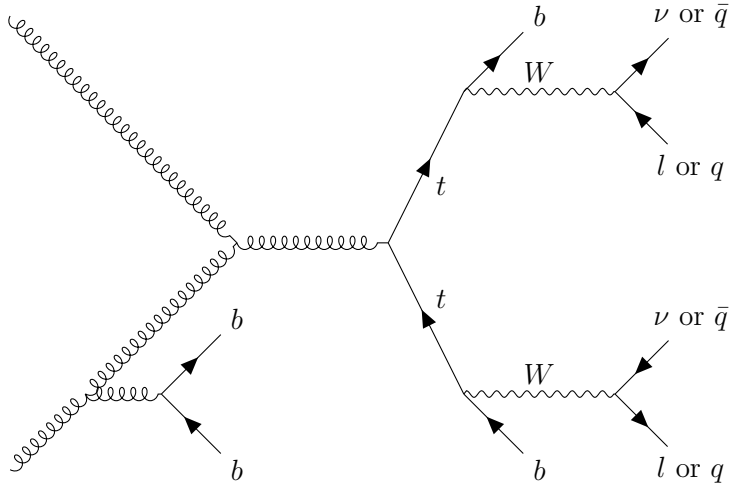

Figure 8.2. Feynman diagram for an example of production of $t\bar{t}$ with heavy flavor radiation.

8.2 Monte Carlo simulation

The simulated events are generally produced in three stages; generation of the hard scattering process, particle showering, and detector simulation (see section 4.7).

There are several public codes for MC event generation and showering, the choice of generator for a particular background is done based on theorist recommendations and the ability to reproduce the distributions in data. The comparison of real data and MC events is always first done "blind", which means that data is not used in signal sensitive regions.

8.3 $t\bar{t}$ modeling

The $t\bar{t}$ background was generated at NLO with PowhegBox 2.0 using the CT10 PDF set. The showering was done using Pythia, version 6 [83] for Paper II and Paper III, and 8 [58] for the current unpublished analysis. The samples were renormalized to the NNLO prediction of Top++ 2.0. The "vanilla" version of $t\bar{t}$ samples for any of the generators tested show some disagreement with data, therefore a series of weights are derived to create a sample that best match data or theory predictions.

For $t\bar{t}+light$ and $t\bar{t}+c$ a generator level reweighting is applied to the p_{T} of the top (and anti-top), and then to the $t\bar{t}$ system. In Paper II the weights were derived from measurements of the $t\bar{t}$ inclusive cross section at 7 TeV, while in Paper III they were derived from NNLO calculations. The $t\bar{t}+b$ events are further divided into subcategories by matching the reconstructed jets to MC truth particles. The reconstructed jets can be matched to either a single b-quark or a $b\bar{b}$ pair, labeled as b-jets or B-jets respectively. An event is then labeled based on the matching of the jets not originating from the top decays as $t\bar{t}+b$ or B for events with one extra jet, $t\bar{t}+bb, bB$ or BB for events with two extra jets and so on. Each of these categories are then reweighted to NNLO predictions from SHERPA [59] + OpenLoops [84] samples.

8.4 Event and object selection

The analyses used single lepton triggers for the event preselection, the specific triggers vary depending on the period of data taking as they are optimized for the energy and luminosity of the beams, and are summarized in table 8.1. Triggers with low p_{T} thresholds also require the lepton to be isolated to reduce false positives from fakes and non-prompt leptons. These triggers have lower efficiency for high p_{T} leptons and are therefore used in combination with triggers with no or looser isolation criteria but higher thresholds.

Additional selection criteria for the offline reconstructed leptons include that they have a $p_{\mathrm{T}} > 25$ GeV and are matched to the trigger. Since the electrons are reconstructed from clusters in the EM calorimeter and inner detector tracks, they are required to not lie in the region where the EM calorimeter lacks coverage ($1.37 \leq |\eta| \leq 1.52$). The reconstructed leptons must also have tracks originating from the primary vertex, i.e. the vertex with the highest scalar sum of squared track-p_{T}. In 2012 data, the lepton tracks were required to have a longitudinal impact parameter $|z_0| < 2$mm. In 2015 and 2016 the track were required to fulfill $|z_0 \sin(\theta)| < 0.5$ mm as well as having a significance of the transverse impact parameter,$d_0/\sigma(d_0)$, less than 5 for electrons and less than 3 for muons.

The jets are reconstructed using the anti-k_{T} algorithm [53] with a radius of 0.4 and required to have a p_{T} greater than 25 GeV as well as to lie within $|\eta| < 2.5$. A jet is considered b-tagged if the tagging MVA score passes the 70% working point.

Since an electron can be reconstructed as a jet from the clusters in the EM calorimeter, any jet within $\Delta R < 0.2$ of an electron is removed. Leptons can also originate from semileptonically decaying hadrons, and thus any electron or muon within $\Delta R < 0.4$ of a jet passing the selection criteria are then removed as well.

The final event selection requires exactly one (two) leptons and at least five (three) jets with at least three (two) b-tags for the single lepton and dilepton final states. The dataset is then divided into regions based on jet and b-tag multiplicities, a region is called a signal region if it has a sizable fraction of expected signal events compared to the background.

Table 8.1. *Transverse momentum (energy) thresholds for the single muon (electron) triggers used during the different data taking periods.*

Trigger	2012	2015	2016
μ isolated	24 GeV	20 GeV	24 GeV
μ non-isolated	36 GeV	40 GeV	50 GeV
e isolated	24 GeV	24 GeV	24 GeV
e non-isolated	60 GeV	60 GeV	60 GeV
e loose-ID	-	120 GeV	140 GeV

8.5 Signal to background discrimination

The signal sensitivity of the fit depends on the separation of signal and background in the distribution that is fitted. In a search with a complex topology and backgrounds that closely mimic the signal, several variables can offer complementary separation power. It is therefore desirable to combine these variables into a single discriminant. A common technique

is to use so called Boosted Decision Trees(BDT) [85]. A decision tree is essentially a series of cuts on input variables that classifies an event as either signal- or background-like. The optimization of these cuts are performed by "training" the tree with MC data for the signal and background. Training a single tree would maximize the separation for that particular tree, however, one can achieve better overall signal to background separation by using boosted decision trees. Boosting is the process where after a tree has been trained, the events that were missclassified are given a higher weight and a new tree is trained using the same input data, this is then repeated a number of times. The final discriminant, the BDT output variable, is then a weighted average of the separate decision tree classifications. This turns the binary classification (signal or background) into a continuous one, where the scale is arbitrary. Usually the output is binned in a histogram from -1 to 1 where a lower score means more background like. The training of the BDTs for the analyses described here were all done using the TMVA framework[85]. Since the process of boosting trees strive to classify as many events as possible correctly it is sensitive to statistical fluctuations. If the number of events are limited it is possible to train a BDT to recognize features not present in the true distribution, this is called "overtraining". The training of a BDT is therefore tested on an independent sample of the same signal and background processes, in the ideal case the distribution for the BDT output should then be the same in both the training and testing case. Since the overtraining skews the weights given to each tree output, it usually results in a lower separation when tested on a sample that doesn't have the same fluctuations. To avoid overtraining, one can optimize parameters such as the number and size of the trees, and the rate at which the weights grow with each new tree.

8.6 Hypothesis testing and statistical analysis

The searches are compared to the standard model prediction using a binned maximum likelihood fit [86]. The probability of observing a number n events in a single histogram bin is Poisson distributed

$$P(n|\boldsymbol{\theta}) = e^{-\lambda}\frac{\lambda^n}{n!} \tag{8.1}$$

where λ is the expected event rate and is a function of the set of so called nuisance parameters $\boldsymbol{\theta}$. A nuisance parameter is used for each systematic uncertainty that may alter the expected event rate. The nominal value and gaussian $\pm 1\sigma$ variations are derived from MC data to construct a prior probability of measuring a specific value of the parameter $P(\theta_i)$. When testing a signal hypothesis, the event rate is the sum of the event

rate for the signal and background.

$$P(n|\mu,\boldsymbol{\theta}) = e^{-(\mu\lambda_s+\lambda_b)}\frac{(\mu\lambda_s+\lambda_b)^n}{n!}, \tag{8.2}$$

where μ is a parameter known as the signal strength, which should be fit to zero if no signal is present and one for the nominal signal hypothesis. Note that both the signal and background event rates are functions of nuisance parameters, although not necessarily the same ones. For example the expected event rate for both signal and background are dependent on the luminosity measurement, but the signal rate is not dependent on the choice of generator for the $t\bar{t}$ MC data. The likelihood of a signal strength given the experimental result for one bin is

$$L(\mu,\boldsymbol{\theta}|n) = e^{-(\mu\lambda_s+\lambda_b)}\frac{(\mu\lambda_s+\lambda_b)^n}{n!}\prod_i P(\theta_i). \tag{8.3}$$

The total likelihood is the product of all the bins likelihood in all the signal and control regions. The best estimate for the signal strength, $\hat{\mu}$, is found at the maximum of this likelihood. A test statistic $\Lambda(\mu)$ is defined to test a value of the signal strength as the ratio of the likelihood from a conditional fit, where μ is fixed, and an unconditional fit where μ can float freely.

$$\Lambda(\mu) = \frac{L(\mu,\hat{\hat{\theta}})}{L(\hat{\mu},\hat{\theta})} \tag{8.4}$$

where $\hat{\hat{\theta}}$ and $\hat{\theta}$ are the values for the nuisance parameters that maximize the conditional and unconditional likelihoods respectively. $\Lambda(\mu)$ ranges between 0 and 1, with 1 signifying good agreement between the hypothesis of μ and the observed data. Computationally it is more suitable to use the logarithm of the likelihood in the test and it is customary to use the statistic

$$q_\mu = -2\ln(\Lambda(\mu)), \tag{8.5}$$

which for large sample sizes is approximately distributed as a non-central χ^2 function, assuming that the estimate $\hat{\mu}$ is gaussially distributed around the true signal strength. The probability of the hypothesis with signal strength μ being true while observing the estimate $\hat{\mu}$, called the p-value, is then calculated as

$$p_\mu = \int_{q_\mu}^{\infty} f(q_\mu|\mu)dq_\mu, \tag{8.6}$$

where $f(q_\mu|\mu)$ is the probability density function for q_μ. In particle physics it is common to quote the significance Z_μ of the likelihood test. It is defined as the quantile of the normal distribution, i.e. number of

standard deviations, above which the cumulative distribution Φ is equal to $1-p_\mu$

$$Z_\mu = \Phi^{-1}(1-p_\mu). \tag{8.7}$$

Discovery of a new signal is claimed if the significance when setting $\mu = 0$ is greater than five standard deviations. If no deviation from the expected background is found, we want to quantify the certainty with which we can exclude the signal hypothesis. In the searches presented in this thesis, this corresponds to setting an upper limit on μ, since a signal would yield an excess of events. An upper limit can be determined as the largest μ for which the p-value is smaller than some confidence level α, e.g. finding the μ for which $p_\mu < 0.05$ excludes signal plus background hypotheses with strengths above μ with a confidence level(CL_{s+b}) of 95%. Since the background yield might fluctuate downwards, this approach can result in excluding a valid signal hypothesis, especially when the signal and background are poorly separated. To account for this possibility we use the modified frequentist "CL_s" method [87] and a signal strength is instead said to be excluded with a CL_s^α when

$$\frac{p_\mu}{p_0} < \alpha, \tag{8.8}$$

i.e. the p-value for the signal and background hypothesis is weighted by p-value for the background only hypothesis. This has the effect of producing more conservative upper limits when the background is subject to large systematic uncertainties and/or the signal and background are similarly distributed.

As mentioned earlier the pdf $f(q_\mu|\mu)$ is approximated to be a non-central χ^2 distribution, however, its shape depends on the variance of $\hat{\mu}$ which is unknown. To obtain it one can use an "Asimov dataset"[86] which is an artificial dataset constructed so that the estimate of the parameters take on their "true" values (i.e their nominal values from MC data). The test statistic can then be calculated using the Asimov dataset

$$q_\mu^A = -2\ln\frac{L(\mu,\hat{\hat{\boldsymbol{\theta}}})}{L(\mu',\boldsymbol{\theta})} \approx \frac{\mu-\mu'}{\sigma^2}, \tag{8.9}$$

where μ' is the nominal value for the signal strength and σ^2 is the variance of $\hat{\mu}$. The approximation is what leads to the non-central χ^2 pdf. It is then straightforward to extract the variance on $\hat{\mu}$ depending upon which hypothesis is being tested:

$$\sigma^2 = \begin{cases} \frac{\mu'^2}{q_0^A} \text{ for discovery} \\ \frac{\mu^2}{q_\mu^A} \text{ for exclusion} \end{cases}. \tag{8.10}$$

8.7 8 TeV search

The first ATLAS search for $H^+ \to tb$ was performed with 20.3 fb^{-1} of 8 TeV pp collision data collected in 2012, this search was published in Paper II, it looked for charged Higgs bosons in the mass range 200-600 GeV in the single lepton channel.

The signal Monte Carlo data was modeled using next to leading order 5FS calculations with the POWHEG BOX generator and showering with PYTHIA 8.1. Samples were produced for 11 values of the charged Higgs boson with intervals of 25 GeV up to $m_{H^+} = 300$ GeV and 50 GeV thereafter. All samples were produced assuming a zero width[1] of the charged Higgs boson. This assumption is deemed valid as the mass resolution of the search is very broad, $\mathcal{O}(50)$ GeV at the lowest masses and even larger at higher masses.

Events were selected for the analysis by requiring exactly one lepton and at least three jets including two tagged as b-jets. These events were then categorized into four control regions and one signal region. The signal region requires at least five jets of which at least three must be tagged as b-jets. The most discriminating single variable is the H_T, and is used in the control regions for the fit. In the signal region a BDT was used. Two alternative BDTs were trained, one against $tt + b$ and one against the inclusive background. It was found that the one trained against $tt + b$, referred to as the HF-BDT, reduced the anti-correlation between the signal strength and the $tt + b$ scale factor. The data was fit to the MC prediction of the H_T in the control regions and the BDT output in the signal region using a binned likelihood fit.

The largest systematic uncertainties come from the modeling and normalization of the $t\bar{t}$+HF; a 50% uncertainty was applied to the $tt + b$ and $tt + c$ cross sections; For $tt + c$ the difference between applying the top and $t\bar{t}$ p_{T} reweighting were used as a two separate systematics;

The signal strength was fit as larger than zero for all masspoints other than 600 GeV. The largest deviation from the background only hypothesis was at 250 GeV, with as local significance of 2.4 sigma. Such a broad excess is not compatible with a signal, as made evident by injecting a signal and evaluating the expected upper limits at neighboring mass points. Figure 8.3 show the expected and observed limits, as well as the expected limits for a $m_{H^+} = 300$ GeV signal, which best matched the observations. This excess is most likely a systematic shift caused by bad modeling of the $t\bar{t}$+HF background.

[1] The width,Γ, of a particle is the inverse of its lifetime, $\Gamma = \hbar/\tau$.

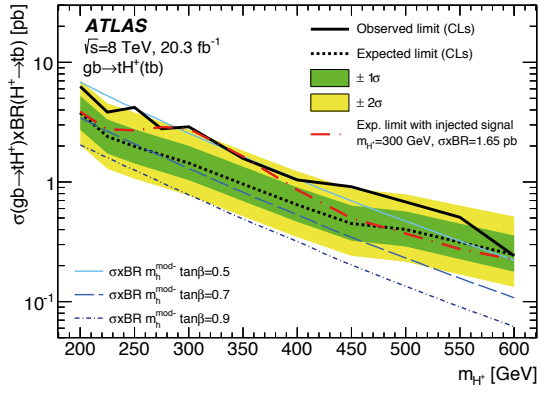

Figure 8.3. The expected and observed 95% CL_S upper limits on the cross section times branching ratio for $H^+ \to tb$ for the 8TeV analysis in Paper II. The red dashed curve show the expected limits if a 300 GeV H^+ signal was present.

8.8 13 TeV searches

This search used 13.2 fb^{-1} 13 TeV data collected in 2015 and 2016 and looked for charged Higgs bosons with masses ranging from 300 to 1000 GeV. The results were published as a note for the ICHEP 2016 conference and will hencefort be refered to as the ICHEP16 analysis to differentiate it from the second analysis at 13 TeV using the full 2015+2016 dataset, which is unpublished at the time of writing. The signal MC samples were generated as 4FS with MG5_aMC@NLO and showered with Pythia 8. The change to 4FS compared the 5FS as in the previous analysis was prompted by theorist recommendations[88], which is expected to better model the b-jet kinematics in the final state. This meant that the signal region ($\geq 5j \geq 3b$)[2] could be split into more regions with exclusive b-jet requirements. The cross section is still computed using a Santander matching of the 4FS and 5FS. The signal regions used were $5j3b$, $5j \geq 4b$, $\geq 6j3b$ and $\geq 6j \geq 4b$.

The normalization of the $t\bar{t}$+HF components were left as floating parameters, to let the fit adjust for the underestimate compared to data. The expected and observed limits are shown in figure 8.4. The largest deviation from the background only hypothesis is found at 600 GeV, corresponding to a local significance of 2.1 standard deviations.

[2]Here, a more compact notation is used where j means any jet and b means a jet that has been tagged as a b-jet

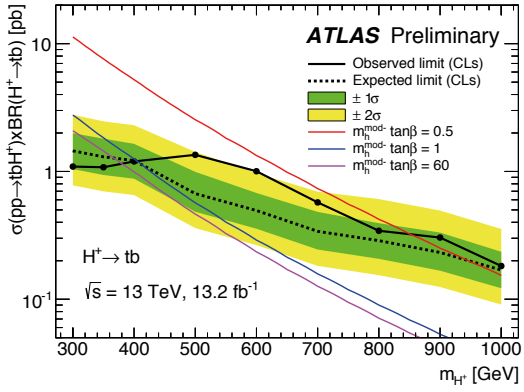

Figure 8.4. The expected and observed 95% CL_S upper limits on the cross section times branching ratio for $H^+ \rightarrow tb$ for the ICHEP16 analysis in Paper III.

8.9 Dilepton analysis

The dilepton final state can increase the sensitivity of a $H^+ \rightarrow tb$ search when combined with the single lepton channel. It can also be used as a cross check with the single lepton channel if a signal is observed. The largest draw back of this final state is the much smaller branching ratio, the low yield means that statistical errors will be large. For the ICHEP16 analysis the signal samples were produced inclusively, that is with both single and dilepton events according to the branching ratios. The low number of dilepton MC events meant that there ware large statistical uncertainties, and we had to use one inclusive signal region $\geq 3j \geq 3b$. Using more regions with exclusive b-tag requirements can help constrain the $t\bar{t}$+HF background, as seen in the single lepton channel. When performing Asimov fits in the dilepton channel it was found that the normalization of the $t\bar{t}$+HF components were heavily anti-correlated with the signal, as large as 80% at the low masspoints. This is not surprising since the background and signal are so kinematically similar, and thus the BDT does not offer much separation. However, since the normalization was left floating a large anti-correlation meant that the fit could easily "inflate" a (perhaps non-existent) signal just by pulling down the $t\bar{t}$+HF and replacing it with signal and still agree with data. For that reason the dilepton channel was left out of the ICHEP16 analysis.

For the following analysis a dedicated dilepton MC sample was produced with a number of events comparable to that of the single lepton channel. The signal region was then split into $3j3b$, $\geq 4j3b$ and $\geq 4j \geq 4b$. The sensitivity in these regions, quantified by the signal yield divided by the square root of the background yield, is shown in figure 8.5. The $3j3b$ region is mostly sensitive to lower masspoints, in fact it has a lower

$S/\sqrt{B}$ than the $4j2b$ region for charged Higgs bosons masses above 800 GeV. This is partly due to the fact that the b-quarks from the gluon splitting get higher p_{T} (since one of them must fuse with a top and produce the heavier H^+). These jets can then pass the object cuts more often, and more events end up in the $4j$ regions. The b-quark from the H^+ decay is also expected to be produced with low p_{T} at lower H^+ masses as most of the energy goes to the mass of the top, which means that is is often lost in the cuts on jet p_{T} and only 3 jets are found in low mass H^+ events. Another reason the yields at higher masspoints reduce is that the analysis only considers small radius jets. When a particle decays, the decay products carry the momentum and if the particle is significantly heavier than the decay products they will emerge from the decay in a colinear fashion. With limited detector resolution a decay from a heavy object can look like one "fat-jet" with large radius rather several smaller ones. For the charged Higgs boson the threshold where this becomes a significant effect is around $m_{H^+} \approx 1$ TeV.

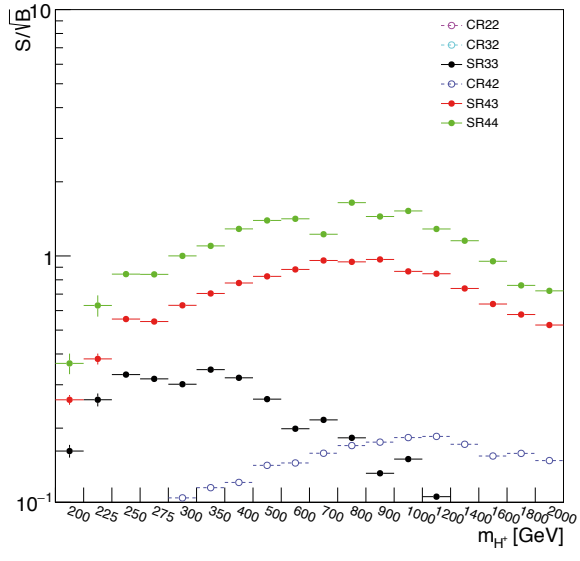

Figure 8.5. The signal over square-root of background yields in the dilepton signal and control regions as a function of the H^+ mass. The y-axis has been normalized to an arbitrary integrated luminosity.

8.9.1 Variable selection

To train a BDT input variables are selected that have the best separation between signal and background. These variables are often based on intuition and knowledge about the physical process at hand, e.g. the leading b-jet p_{T} is expected to be larger for a heavy charged Higgs event than for the average $t\bar{t}$ event. However with several jets and leptons in the event the kinematical combinations are many and the optimal variables to use are not obvious. In an attempt to automate the selection of variables and get the best possible separation, a method to evaluate a large number of variables quickly was devised. The four momentum reconstructed objects (jets,leptons and transverse missing energy) were combined in all possible permutations, e.g P_{jet1}, $P_{jet1} + P_{lep1}$, $P_{jet1} + P_{lep1} + E_T$ et.c, where the subscript denotes the leading jet or lepton in terms of p_{T}. This leads to a list of four vectors, some with more physical meaning than others, from which some simple variables can be constructed; p_{T}, η, invariant mass and energy. More variables can be formed by taking two of these objects and calculating the difference in p_{T}, η, ϕ,energy and invariant mass.

The total number of variables are several thousand. A BDT can in theory handle a lot of variables, but since we want to be able to check the validity of each variable in data it is only feasible to use about ten variables for a training. To ensure the absolute best separation of the BDT output one should train a BDT for each subset of variables. This is however extremely time consuming. Instead the variables were evaluated one by one by calculating two metrics; the separation $< S^2 >$ and the integral under a ROC[3] curve. The separation of signal and background histograms is defined as

$$< S^2 >= \frac{1}{2} \sum_{i=1}^{N_{bins}} = \frac{(y_s - y_b)^2}{y_s - y_b}, \tag{8.11}$$

where $y_{s,b}$ are the yields of the signal and background in bin i and ranges between zero (complete overlap) and 1 (complete separation). This metric is used internally by TMVA to optimize the cuts in the training of a BDT. The ROC curve is found by plotting the signal efficiency against the background rejection for a varying cut on the variable, e.g for a variable ν:

$$eff_s(x) = \frac{n_s(\nu > x)}{n_s^{tot}} \tag{8.12}$$

$$rej_b(x) = 1 - \frac{n_b(\nu > x)}{n_b^{tot}} \tag{8.13}$$

[3]ROC stands for receiver operating curve, a name that comes from it's early use in military radio operations. The method has later found widespread use in evaluating classifiers in many fields.

where $n_{s,b}(\nu > x)$ stands for the number of signal or background events passing the cut $\nu > x$. The reason for using both of these metrics is that $< S^2 >$ was found to best predict the variables that will have a large impact on the BDT separation, however it is very susceptible to statistical fluctuations and histogram bin resolutions. It often assigned a large value to a variable that was clearly only separated from background by noisy bins. The ROC integral is a more reliable metric since random fluctuations only matter at the ends, i.e where the efficiency or rejection is calculated for a few bins in the histograms. The variables where thus ranked by according to final score by multiplying these two metrics together. An example of the separation on ROC curve is shown for two variables in figure 8.6.

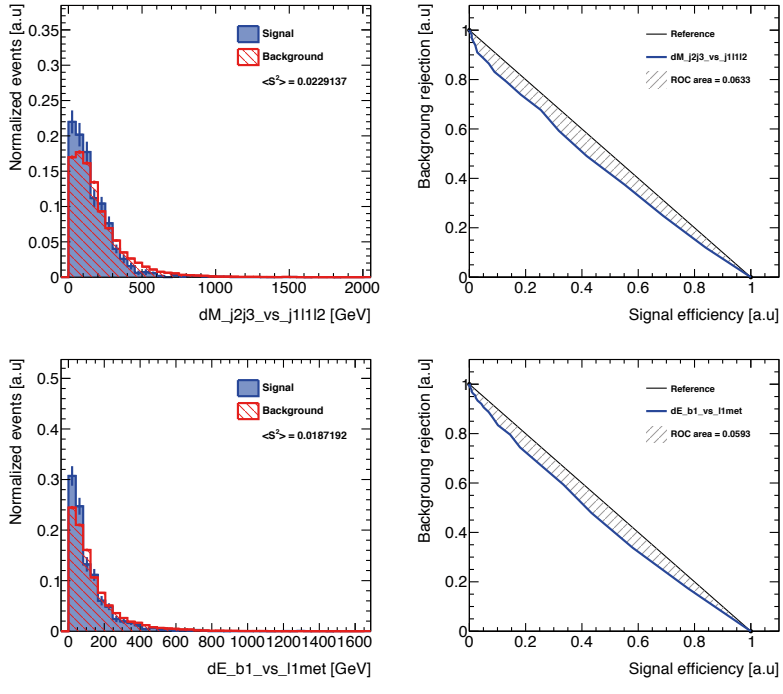

Figure 8.6. The separation $< S^2 >$ and the ROC area for the best variables in the $4j3b$ region.

The list of ranked variables were topped by variables that were very similar, and highly correlated. Even though BDTs can make use of the correlation between variables in signal and background, these variables are in a sense holding the same information and the point of this exercise was to find variables that could combine into a better classifier. For the ICHEP16 analysis each masspoint was optimized by simply starting with the highest ranked variable and then removing any variables with a linear

correlation higher than 50%. Then move on to the next best remaining variable until a list of 10 variables had been found. For the following analysis it was decided to try to harmonize the variable selection over the mass range and another approach was used. After a ranking list of variables had been produced for a mass point the variables, instead of removing correlated variables they were put in a group. The final variable list was then produced by taking the variable with the best mean ranking for all the masspoints and which ever group it belonged to was noted. Since the correlations, and thereby grouping, are different from each masspoint, each group was allowed to be used twice before being discarded. This process was repeated until the list of variables had been exhausted, which lead to lists of about 5 to 10 variables for the different signal regions. A cut was made at 600 GeV, since the kinematics are so different for a lighter and heavier H^+, so that there was a low-mass and high-mass set of variables for each region.

8.9.2 Mass reconstruction

The prospect of being able to reconstruct the charged Higgs boson mass is enticing since it should be a clear way to distinguish signal and background events. With two neutrinos in the event this is not an easy task however since the direction of the individual neutrinos can't be measured. In the following section an reconstruction technique similar to the missing mass calculator [89] used in the SM $h \to \tau\tau$ analyses is evaluated for the $H^+ \to tb$ search. If we assume the lepton and neutrino come from a W decay and the p_T of the neutrinos are known, the mass of the W can be used to constrain the p_{z} of the neutrinos. In case of one neutrino, the missing transverse energy would give a good indication of its p_{T}, but with two momenta combining to the E_{T}^{miss} extra information is needed. The p_{T} of the neutrinos should combine in some way to give the total missing energy;

$$\begin{cases} p_{\mathrm{T}}^1 = \rho E_{\mathrm{T}}^{miss} \\ p_{\mathrm{T}}^2 = (1-\rho) E_{\mathrm{T}}^{miss} \end{cases} \text{where } 0 \leq \rho \leq 1. \tag{8.14}$$

The p_T of the neutrinos should however be correlated to the p_{T} of the leptons, since in the rest frame of the W they are propagating in opposite directions. A probability density function(PDF), $f(q)$, can be produced for the ratio of the p_{T} of the neutrino and lepton from the W, where

$$q = \frac{p_{\mathrm{T}}^{\nu}}{p_{\mathrm{T}}^{lep}} \tag{8.15}$$

Using this function, each possible value of the neutrino p_{T} can be assigned a weight from the observed lepton p_{T}. Since the resolution of the W mass

is limited, a PDF can also be used for the reconstructed W mass. The reconstruction can then be given a total probability

$$P = \int_0^{2m_W} \int_0^{10} \int_0^1 f(m_W) f(q) dm_W dq d\rho, \tag{8.16}$$

where the p_{T} ratio q is integrated over a range that covers the full pdf, e.g. 0-10 here. The PDFs were derived from MC simulations by matching truth and reconstructed objects, and stored as histograms. The integration in equation 8.16 then becomes a sum of probabilities where each term is

$$P_i(m_W, q, \rho) = h(m_W)h(q)h(\rho) \tag{8.17}$$

where $h(x)$ denotes the probability of the bin containing that value. The most probable values of m_W, q and ρ for an event is then found by "integrating" over all the histograms and noting them at the largest P_i. From the values it is then straight forward to kinematically reconstruct the H^+ and calculate its mass, given the correct b-jets from the decay. A complication not yet mentioned is the possibility of combining the wrong jets and leptons. For an event with four b-jets there are twelve possible jet assignments, and two possible lepton assignments, which makes the total number of permutations 24. In order to select the correct permutation, an extra PDF for the top mass was also used, which can be used for the two tops in the process. The idea being that the correct permutation would have the highest P_i by reconstructing the tops correctly. As it turned out the correct permutation was only chosen in about 25% of all events, with the effect that the reconstructed H^+ mass offered no separation from the $t\bar{t}$ background. If the correct permutation could be found, this method does a reasonably good job at reconstructing the mass as can be seen in figure 8.7.

A similar method has recently been developed for the single lepton final state. In this method no attempt is made to find the correct permutation but each one is included in a likelihood computation. This method has proven to have good separation power at low masses. The permutation weighting has yet to be tested with dilepton final state reconstruction, but might will be evaluated for future analyses.

8.10 Conclusions for the $H^+ \to tb$ searches

Two searches for $H^+ \to tb$ in the single lepton final state were presented. The searches were performed using data corresponding to an integrated luminosity of 20.3 and 13.2 fb^{-1} gathered with the ATLAS detector at collision energies of 8 and 13 TeV respectively. Neither analysis found any evidence for a charged Higgs boson in their mass search window. Both

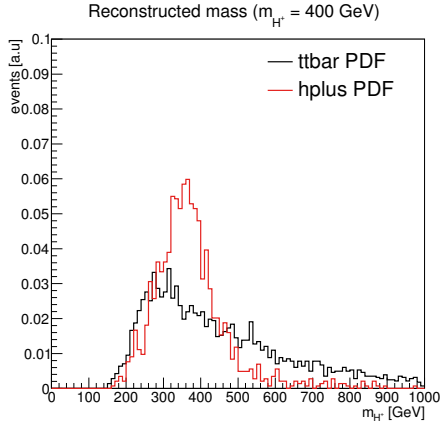

Figure 8.7. The reconstructed H^+ mass (red) when the correct b-jet and lepton permutation is used, the distribution for $t\bar{t}$ uses the permutation with highest probability.

searches were based on using BDTs to separate signal from background in the signal regions and a binned maximum likelihood fit to data. The 8 TeV analysis put 95%CL_s upper limits on $\sigma(pp \to tH^+) \times BR(H^+ \to tb)$ between $6-0.2$ pb for charged Higgs boson masses between 200-600 GeV. The observed limits were higher than expected from the SM background only hypothesis but incompatible with a signal from a charged Higgs boson. The 13 TeV analysis used an updated background model and signal Monte Carlo simulation. The observed upper limits ranged between 1-0.2 pb for m_{H^+} = 300-1000 GeV. The main background of the analysis is $t\bar{t}$ with additional heavy flavor radiation. The modeling of this background and uncertainties related to the b-tagging stand for the largest systematic uncertainties to the limits. Since the systematic uncertainty is also larger than the statistical uncertainty, future ATLAS searches in this channel can only make marginal improvements off the limits unless these systematical uncertainties are constrained. Including the dilepton final state offers another measurement which, when combined with the single lepton channel, could result in a better handle on the background processes and an overall increase in sensitivity. Analysis methods for the dilepton final state has been developed and will be used in the search using the full 2015-2016 dataset, which is being finalized at the time of writing.

Part IV:
Summaries and outlook

9. Conclusion

The goals of the ATLAS experiment is to provide experimental observations that can help us build better models of particle physics. Such observations include precision measurements of previously known processes as well as evidence for new particles or interactions. The high energy of the LHC proton-proton collisions makes it hypothetically possible to produce new particles too massive to have been produced at previous collision experiments. The search for new particles is motivated by the inability of the standard model(SM) to describe such things as dark matter, and the observations of neutrino oscillations. This thesis focuses on the search of a charged Higgs boson, a hypothetical particle that emerges in many extensions to our current model, including supersymmetry(SUSY). The SUSY models proposes that every known particle has a partner, differing by the quantum number "spin". These SUSY particles could be a candidate for dark matter. Searches for the charged Higgs boson has been performed by other experiments and has mostly ruled out the existence of a new particle with mass lower than the top quark. The searches presented in this thesis provide improved limits on the production of heavier charged Higgs bosons decaying into a top and bottom quark pair. Since no evidence for a new particle was found, these upper limits can be used to constrain the proposed models and guide the future of both theoretical and experimental endeavors in the field of particle physics.

The LHC is also capable of providing particle collisions at a very high rate, and after the upgrade to the High Luminosity LHC(HL-LHC) the experiments will have an excellent opportunity to make further precision measurements of the SM and search for very rare processes. In fact, the number of events that are produced is so large that the experiments must select which events to store and analyze, in a few seconds after the collision. The ATLAS detector, as it functions today, can not handle the high collision rate of the HL-LHC. The large number of simultaneous collisions, so called pile-up, would saturate parts of the detector and make it difficult to recognize the interesting events. The triggers that select the events to store must be improved to reject more of the uninteresting events without discarding the ones of interest. The selection of events is done using a series of triggers in escalating complexity, and in the current detector the information form the inner detector and the trajectories(tracks) of particles are used later in this sequence. This thesis considers the design of a hardware track trigger, bases on pattern matching followed by a linear fit,

that would operate with a latency of a few tens of microseconds. By simulation, this trigger has been shown to be efficient at rejecting background events at a rate sufficient for the HL-LHC, while keeping the efficiency for signal events and respecting the latency and hardware constraints. This hardware track trigger is an option for the upgrade to the ATLAS detector, but the methods are general enough to be applicable outside of high energy physics. The ability to recognize features in data at a high speed is desirable in many evolving technologies such as self driving cars, speech recognition and image processing.

Sammanfattning på Svenska

Fysik och vetenskap i allmänhet handlar om att bygga modeller och formulera teorier som kan beskriva och förutsäga vårat universum såsom vi upplever det. Ett annat viktigt inslag i vetenskapen är att försöka förbättra precisionen hos dessa förutsägelser och att leta efter bakomliggande egenskaper hos våra modeller, att leta efter de mest grundläggande beskrivningarna av naturen. På en mänsklig skala, utgör Newtons lagar om rörelse och gravitation en modell genom vilken mycket av den dagliga fysiken kan beskrivas. Den kan beskriva hur två massiva föremål attraheras av varandra genom tyngdkraften, men för att förstå varför två föremål av samma storlek men olika material kan ha olika massa, måste vi titta på en mindre skala. Genom att formulera en modell för de ingående atomerna och molekylerna, får vi en bättre förståelse av objektets egenskaper. Partikelfysiken syftar till att bygga en modell för den minsta skala vi för närvarande känner till, vi talar om "elementära" eller "fundamentala" partiklar: de minsta byggstenarna i atomer och interaktions medierande partiklar som ger upphov till de krafter som håller atomkärnor tillsammans och elektromagnetiska fenomen. En sådan modell är inte bara viktig för att kunna beskriva universum som vi ser det idag, men också för att förstå dess ursprung. Jämfört med stunderna just efter big bang är vårt nuvarande universum i ett svalt, lågt energitillstånd. Många av de fundamentala partiklarna hittas endast i bundna former, såsom protoner vilka är uppbyggda av kvarkar och hålls ihop av den starka kraften. Det tidiga universum var mycket varmare och tätare, vilket betyder att protoner kunde inte bildas utan att de skulle vara så energiska att de bröts upp igen. Dessa förhållanden kan återskapas idag genom att kollidera partiklar med höga energier. Large Hadron Collider (LHC) vid CERN kolliderar protoner med den högsta energin som någonsin uppnåtts i ett sådant experiment. Det finns flera saker som den nuvarande modellen för partikelfysik inte kan förklara, Såsom förekomsten av mörk materia eller obalansen mellan materia och anti-materia i universum. Genom att undersöka resultaten av proton-proton kollisioner hoppas vi få insikt i de fysiska processerna under universums tidiga ögonblick och hur det utvecklats till det tillstånd vi ser idag.

ATLAS-experimentet är en av flera partikeldetektorer vid LHC. Det är en detektor som är konstruerad för att både göra precisionsmätningar av den nuvarande modellen och att söka efter nya partiklar. Denna avhandling presenterar sökandet efter en hypoteserad partikel, en laddad Higgs

boson, utfört med data som samlats in med ATLAS-detektorn vid kollisions energier påbåde 8 och 13 TeV, samt arbetet med att förbereda uppgraderingen av detektorn.

Under 2012 meddelade ATLAS- och CMS-experimenten upptäckten av en ny partikel, en Higgs boson. Denna partikel var hypoteserad under 1960-talet och dess underliggande Higgs mekanism förklarar hur elementŕa partiklar får sin massa. Standard modellen, med en Higgs boson, kan fortfarande inte förklara ovannämnda kosmologiska observationer. En elektriskt laddad Higgs boson förekommer i många förslag till nya modeller, inklusive supersymmetri. I en supersymmetrisk teori har alla partiklar i standard modellen en super-partner, en partikel som skiljer sig i kvanttalet "spin". Dessa super-partners skulle kunna vara kandidater till mörk materia. Egenskaperna hos en laddad Higgs boson, t.ex. dess massa och hur den interagerar med andra partiklar är inte fixerat av teorin men bildar ett parameterrum där vi måste leta efter den. Sökningar efter laddade Higgs bosoner har utförts före LHC, utan att finna några, men med den nya energin hos LHC har experimenten kunnat söka efter mer massiva partiklar. I det här arbetet letade vi efter en laddad Higgs boson som söderfaller till de tyngsta två kvarkarna, ett par av topp- och botten-kvarkar. Detta är det sönderfall som förväntas ske oftast i många hypoteser, om den laddade Higgs bosonen har en massa som är större än top kvarkens massa. Data analyserades med hjälp av multivariata tekniker för att separera signal- och bakgrunds-liknande händelser och jämfördes med simuleringar i en statistisk analysis. Inga signifikanta avvikelser från standardmodellen hittades i de data som samlats in fram till 2016 och därmed kan vi sätta övre gränser för produktionen av en laddad Higgs boson. Dessa gränser kan sedan användas för att utesluta delar av parameterrummet.

LHC kommer att uppgraderas runt 2025 för att öka luminositeten, det vill säga intensiteten hos proton strålarna, vilken kan jämföras med ljusstyrkan i en stråle av ljus. Anledningen till denna uppgradering är att med högre luminositet kommer antalet kollisioner öka, och experimenten kommer att kunna förbättra den statistiska säkerheten i sina mätningar samt att söka efter processer som hitills varit allt för sällsynta. Vid LHC accelereras inte protoner en efter en utan i klungor. Luminositeten kan ökas genom att använda fler protoner per klunga men också genom att klämma ihop strålen vid kollisionspunkten. Det betyder att den takt med vilken vi kan hoppas producera sällsynta händelser kommer att öka, men också att bakgrunden ökar. Såkallat pile-up, antalet protonkollisioner per klunga som korsar interaktionspunkten, kommer också att öka. Takten för dessa korsningar vid LHC är för hög för att ATLAS ska kunna läsa och lagra all data för varje händelse, istället använder vi "triggers" som väljer ut händelser som ser intressanta ut. De triggers som används idag passar inte för den höga frekvensen av kollisioner vid Hög Luminositet-LHC

(HL-LHC) efter uppgraderingen och måste således förbättras om experimenten ska kunna dra nytta av den hgre luminositeten. Ett sätt att göra detta är att använda informationen från spårdetektorn som ger information om banorna för laddade partiklar som färdas genom detektorn. Genom att använda algoritmer som kan implementeras i hårdvara kan en spårtrigger vara snabb nog att arbeta inom den korta tid som krävs vid HL-LHC. Spårdetektorn ger rymd-punkter, det vill säga tre-dimensionella mätningar av partikelbanorna vid olika intervaller, till vilka ett spår kan anpassas matematiskt. Spåren från elektriskt laddade partiklar med hög energi utmärker sig genom att de håller sig rakare, jämfört med partiklar med låg energi som böjer sig när de färdas genom det magnetfält som spårdetektorn befinner sig i. Med höga nivåer av pile-up blir mängden data från spårdetektorn mycket stor. Att göra anpassningar till alla kombinationer av rymd-punkter skulle ta för mycket tid, en spår trigger vid HL-LHC bör kunna ge ett beslut (interessant händelse eller inte) inom några mikrosekunder. Därför måste en spårtrigger kunna välja en delmängd av alla dessa rymd-punkter. I denna avhandling undersöks ideen om att först använda nuvarande triggers för elektroner och myoner för att välja en mindre del av spårdetektorn, och sedan jämföra rymd-punkterna i denna del med mönster som motsvarar partiklar med hög energi. Genom att endast utföra spår anpassningar till de rymd-punkter som matchar ett mönster, kan mängden data och tiden för att hitta ett spår reduceras. Resultaten visar att detta är ett gångbart alternativ för att sortera bort bakgrundshändelser samtidigt som hög effektivitet för signaler bevaras, även vid höga nivåer av pile-up.

Summary in English

Physics, and science in general, is about building models and formulating theories that can describe and predict the universe as we experience it. Another key feature of science is to try to improve the precision of those predictions and to look for underlying features of our models, to look for the most fundamental descriptions of Nature. For example, on a human scale, Newtons laws of motion and gravity constitute a model by which much of the day-to-day physics can be described. It can describe how two massive objects are attracted to each other by the force of gravity, but to understand why two objects of the same size but different materials can have different mass, we need to look at a smaller scale. By formulating a model for the constituent atoms and molecules, we get a better understanding of the objects properties. Particle physics aims to build a model for the smallest scale we currently know of, we speak of "elementary" or "fundamental" particles; the smallest building blocks of atoms and interaction mediating particles that give rise to the forces that hold atomic nuclei together and electromagnetic phenomena . Such a model is not only important to be able to describe the universe as we see it today, but also to understand its origin. Compared to the moments right after the big bang, the current universe is in a cool, low energy state, with many of the fundamental particles only found in bound states such as protons which are built up of quarks and held together by the strong force. The early universe was much hotter and denser, which means that protons could not form or they would be so energetic that they broke up again. These conditions can be recreated today by colliding particles at high energies. The Large Hadron Collider(LHC) at CERN collides protons with the highest energy ever achieved in such an experiment. There are several things the current model of particle physics cannot explain, such as the existence of dark matter or the imbalance between matter and anti-matter in the universe. By examining the results of proton–proton collisions we hope to gain insight on the physical process during the first moments of the universe and how it evolved into the state we find it in today.

The ATLAS experiment is one of several particle detectors at the LHC. It is a multipurpose detector built to both do precision measurements of the current model and to search for the existence of new particles. This thesis presents searches for a hypothesized particle, a charged Higgs boson, performed with data gathered with the ATLAS detector, as well as work on preparing the upgrade of the detector.

In 2012 the ATLAS and CMS experiments announced the discovery of a new particle, a Higgs boson. This particle was hypothesized in the 1960's the underlaying Higgs mechanism explains how fundamental particles get their mass. However, the standard model with a single Higgs boson is still not able to explain the aforementioned cosmological observations. An electrically charged Higgs boson is a feature of many suggested extensions of the current model, including supersymmetry. The properties of such a particle, e.g. its mass and how it interacts with other particles are not fixed by theory but forms a parameter space in which we must look for it. Searches for charged Higgs bosons have been performed prior to the LHC, but with the new energy scale of the LHC, the experiments have been able to look for heavier particles. In this work we searched for a charged Higgs boson decaying into the heaviest two quarks, a top and bottom pair. No deviations from the standard model were found in the data gathered up until 2016, and hence we can set upper limits on the production rate of a charged Higgs boson. These limits can then be used to exclude parts of the parameter space.

The LHC will be upgraded around 2025 to increase the luminosity, that is the intensity of the proton beams. Protons are not accelerated one by one at the LHC but in bunches. The luminosity can be increased by using more protons per bunch but also by squeezing the bunches to be smaller at the point of collision. This means that the rate at which we can hope to produce rare events will increase but also that the background rates and so called pile-up, the number of proton collisions per bunch crossing, will increase. The rate of bunch crossings at the LHC is much too high for ATLAS to be able to readout and store all data for each event, instead we use triggers that select events which look interesting. The current triggers are not suited for the high rates and pile-up of the High Luminosity (HL) LHC after the upgrade and must thus be improved. A way to do this is to use the information from the tracking detector that provides information on the trajectories of charged particles. By using algorithms that can be implemented in hardware a track trigger can be made fast enough to work within the short latency required at the HL-LHC. The tracking detector provides space points, measurements of the particle trajectories at different intervals, to which a track can be fitted. The amount of data from the tracker is very large, and performing track fits on all the combinations of the space point would take too much time. Therefore a track trigger must be able to select a subset of space points on which to perform the track fit. For this thesis we have explored the idea of using standalone electron and muon triggers to select a part of the tracker volume, and then select space points that match precomputed patterns that correspond to high energy particles. It has been shown that this is a viable option to reduce background rates while keeping high efficiency for the events we want to keep, even in high pile-up conditions.

Summary in French

La physique et la science en général consiste à construire des modèles et à formuler de théories qui décrivent et prédisent l'univers à mesure que nous l'expérimentons. Une autre caractéristique essentielle de la science est d'essayer d'améliorer la précision de ses prédictions, afin de rechercher les caractéristiques les plus fondamentales de la nature. Par exemple à une échelle humaine, les lois de Newton du mouvement et de la gravité constituent un modèle par lequel une grande partie de la physique du quotidien peut être décrite. Elles décrivent comment deux objets massifs sont attirés l'un par l'autre selon la force de la gravité, mais pour com- prendre pourquoi deux objets de la même taille, faits de différents matériaux peuvent avoir une masse différente, nous devons regarder à une échelle beaucoup plus petite. En formulant un modèle d'atomes et de molécules comme constituants de la matière, nous obtenons une bien meilleure compréhension des propriétés des objets. La physique des particules vise à construire un modèle de la matière à la plus petite échelle que nous lui connaissons actuellement ; nous parlons alors de particules « élémentaires » ou « fondamentales ». Un tel modèle n'est pas seulement important pour décrire l'univers tel que nous le voyons aujourd'hui, mais aussi pour comprendre son origine. Comparé aux premiers instants après le big bang, l'univers actuel a une température beaucoup plus faible, avec des particules fondamentales se trouvant dans des états composites tels que les protons constitués de quarks maintenus ensemble par l'interaction forte. L'univers primitif était beaucoup plus chaud et plus dense, ce qui signifie que les protons ne pouvaient s'y former car ils auraient été immédiatement rompus. Ces conditions peuvent être partiellement recréées aujourd'hui dans les collisions de particules à très haute énergie. Le Grand Collisionneur Hadronique (LHC) du CERN produit des collisions de protons aux énergies les plus élevées jamais réalisées dans une expérience. Il existe cependant plusieurs observations que Le modèle actuel de la physique des particules ne peut pas expliquer : tels que l'existence de la matière noire ou l'énorme déséquilibre entre la matière et l'anti-matière dans l'univers. En étudiant les produits des collisions de protons du LHC, nous espérons mieux comprendre les processus de physique ayant eu cours durant les premiers instants de l'univers, et mieux retracer comment il a évolué vers l'état dans lequel nous le trouvons aujourd'hui. ATLAS est l'une des quatre expériences du LHC. C'est un détecteur polyvalent conçu à la fois pour des mesures de précision du modèle standard et pour sonder l'existence

de nouvelles particules. Cette thèse présente la recherche d'une particule hypothétique : un boson de Higgs chargé, réalisée sur des données recueillies avec le détecteur ATLAS, ainsi qu'un travail destiné à la jouvence du détecteur pour la phase à haute luminosité du LHC. En 2012, les expériences ATLAS et CMS ont annoncé la découverte d'un nouvelle particule compatible avec le boson de Higgs prévu par le modèle standard. Cette particule a été postulée dans les années 1960. Elle explique comment les particules fondamentales obtiennent leur masse. Cependant, la plupart des modèles allant au-delà du modèle standard prédisent l'existence de bosons de Higgs chargés. Les propriétés de telles particules, par exemple sa masse et son couplage aux autres particules, ne sont pas précisément prédites par la théorie, mais constituent un espace de paramètres qui doit être exploré. Des recherches de bosons de Higgs chargés ont été effectuée avant le LHC, cependant l'extension en énergie réalisée par le LHC a permis d'explorer un domaine plus large en masse. Dans ce travail nous avons cherché un boson chargé de Higgs se décomposant en une paire de quarks t et b. Aucun écart par rapport au modèle standard n'a été observé dans les données recueillies jusqu'en 2016, nous pouvons en déduire des limites supérieures sur le taux de production d'un boson chargé de Higgs. Ces limites peuvent alors être utilisées pour exclure des parties de l'espace des paramètres. Le LHC sera mis à niveau vers 2025 pour augmenter sa luminosité (le nombre de collisions par seconde et par cm2). Les protons sont accélérés par paquets. Ainsi, la luminosité peut être augmentée en injectant plus de protons par paquet, mais aussi en focalisant les paquets (réduisant leur taille transverse) au point de collision. Cela signifie que le taux auquel nous pouvons espérer produire des événements rares augmentera, mais aussi que le taux de bruit de fond correspondant à l'empilement (le nombre de collisions moles de protons par croisement) augmentera. Le taux de croisement de paquets au LHC est trop élevé pour pouvoir lire et stocker toutes les don- nées produites. Ainsi nous devons utiliser un système de déclenchement qui sélectionne rapidement les événements intéressants à enregistrer. Le système de déclenchement actuel n'est pas adapté au taux élevé d'empilement attendu pour la phase à haute luminosité (HL) du LHC. Il doit donc être améliorée. Une façon de le faire est d'utiliser les informations du détecteur interne qui fournit des informations sur les trajectoires de particules chargées. En utilisant des algorithmes qui peuvent être mis en œuvre dans l'électronique, un déclenchement de premier niveau sur les traces peut être rendu assez rapide pour fonctionner dans la courte latence requise au HL-LHC. Le détecteur interne fournit des points d'espace, des mesures des trajectoires des particules à des intervalles différents où sont installés des pistes de silicium. La quantité de données du trajectomètre est trop grande, aussi effectuer des calculs sur toutes les combinaisons de points spatiaux prendrait trop de temps. Par conséquent, un déclenchement interne de premier niveau

doit pouvoir sélectionner un sous-ensemble de points spatiaux sur lesquels effectuer le calcul. Dans cette thèse, nous avons exploré l'idée d'utiliser les régions d'intérêt fournies par le système de déclenchement d'électrons et de muons pour sélectionner une partie du volume du détecteur interne, puis de sélectionner les points d'espace qui correspondent aux modèles attendus des traces à haute énergie. Il a été démontré que c'est une option viable pour réduire les taux de bruit de fond tout en gardant une efficacité élevée pour les événements que nous voulons garder, même dans des conditions élevées d'empilement.

Acknowledgments

I would like to thank my main supervisors, Elin Bergeås Kuutmann and Johann Collot, and Richard Brenner and Arnaud Ferrari, who has served as both official and unoffical supervisors at various points during my thesis. You were always helpful and took the time to assist me in all matters from the physics to the move to France.

I would also like to tank the whole Uppsala ATLAS group; Max Isacson and Mikael Mårtensson who I've collaborated closest with on the charged Higgs analyses and the track trigger project; Mattias Ellert who helped me with all matters related to grid computing; All the other current members including Myrto, Pedro, Petar and Tord, as well as the post-docs and PhD students who preceded me Elias, Camilla, Alex, Daniel, and Henrik. You all gave me useful inputs and made the experience of working in Uppsala enjoyable.

I am also very grateful for the two years I got to spend in Grenoble and to all my colleagues there. I would like to give special thanks to Fabienne Ledroit, who helped me with all matters of administration there, and Fairouz Malek who gave me the opportunity to travel to Marocco and initiate collaborations with new people. I would also like to thank my office mates, Clement Camincher and Simon Berlandis, for good discussions both on physics and the French lifestyle.

This thesis would never have been possible without the many people working with the ATLAS experiment, and while they all deserve my gratitude even the smaller groups of the charged Higgs analysis and L1 track project include too many people to name here. Some persons who I've worked closest with are; Xuan Yang and Yang Qin, who also worked on the dilepton channel and I shared much code and many discussions with. Gordon Crone and Francesca Pastore who shared the work of developing the simulation framework for the L1Track trigger. Thank you all for the help on analysis, simulation and reviewing my talks and posters.

I would like to thank the Institut Français Suède, for their generosity by providing me with the ÖMSE travel grant. Being able to travel between the two countries made the collaboration between Uppsala and Grenoble work very well.

Outside of the academic work, this thesis was made possible by my family and friends who supported me. My closest fiends Daniel, Filip, Martin, Nino and Tobias you are all great to hang out with and made me cool down when the work gave me too much stress. Thanks are also

in order for my buddies from university; Anton, Christian, Filip, Fredrik, Rasmus and Simon. Our inter-class discussions were fun and stimulating.

Last, but not least, I am very grateful for the love and support from my mom, dad, sister and family. You have all been a constant source of happiness, inspiration and motivation for me. I could not have done this without you. Thank you.

References

[1] Paul A. M. Dirac. Quantised singularities in the electromagnetic field. *Proc. R. Soc. Lond.A*, 133, 1931.

[2] Carl D. Anderson. The positive electron. *The physical review*, 43(6), 1933.

[3] R. Brout F. Englert. Broken symmetry and the mass of gauge vector mesons. *Phys. Rev. Lett.*, 13(9), 1964.

[4] P. Higgs. Broken symmetries and the masses of gauge bosons. *Phys. Rev. Lett.*, 13(16), 1964.

[5] T.W.B Kibble G.S. Guralnik, C.R. Hagen. Global conservation laws and massless particles. *Phys. Rev. Lett.*, 13(20), 1964.

[6] S. L. Glashow, J. Iliopoulos, and L. Maiani. Weak Interactions with Lepton-Hadron Symmetry. *Phys. Rev.*, D2:1285–1292, 1970.

[7] A. Salam. 8th Nobel Symposium. Almqvist & Wiksell, Stockholm, 1968.

[8] Steven Weinberg. A model of leptons. *Phys. Rev. Lett.*, 19(21), 1967.

[9] C.Patrigiani et al. (Particle Data Group). Review of particle physics. *Chin. Phys.*, C 40(10), 2016.

[10] Super Kamiokande Collaboration. Solar neutrino measurements in super-kamiokande iv. *Phys. Rev. D*, 94(5), 2016.

[11] SNO Collaboration. Combined analysis of all three phases of solar neutrino data from the sudbury neutrino observatory. *Phys. Rev. D*, 88(2), 2013.

[12] Michael E. Peskin and Dan V. Schroeder. *An introduction to Quantum Field Theory*. Westview Press, 1995.

[13] Handbook of LHC Higgs Cross Sections: 4. Deciphering the Nature of the Higgs Sector. 2016. arXiv: 1610.07922 [hep-ph].

[14] LHC Higgs Cross Section Working Group, S. Heinemeyer, C. Mariotti, G. Passarino, and R. Tanaka (Eds.). Handbook of LHC Higgs Cross Sections: 3. Higgs Properties. *CERN-2013-004*, CERN, Geneva, 2013.

[15] UA1 Collaboration. Experimental observation of isolated large transverse energy electrons with associated missing energy at $\sqrt{s}$=540 GeV. *Phys. Lett.*, 122B(1), 1983.

[16] US2 Collaboration. Observation of single isolated electrons of high transverse momentum in events with missing transverse energy at the CERN $\bar{p}p$ collider. *Phys. Lett.*, 122B(5-6), 1983.

[17] UA1 Collaboration. Experimental observation of lepton pairs of invariant mass around 95 GeV/c^2 at the CERN SPS collider. *Phys. Lett.*, 126B, 1983.

[18] UA2 Colaboration. Evidence for $Z^0 \to e^+e^-$ at the CERN anti-p p collider. *Phys. Lett.*, 129B, 1983.

[19] ATLAS Collaboration. Observation of a new particle in the search for the standard model higgs boson with the ATLAS detector at the LHC. *Phys. Lett.*, 716B(1), 2012.
[20] CMS Collaboration. Observation of a new boson at a mass of 125 GeV with the CMS experiment at the LHC. *Phys. Lett.*, 716(1), 2012.
[21] G.C. Branco, P.M Ferreira, L. Lavoura, M.N. Rebelo, Marc Sher, and João P. Silva. Theory and phenomenology of two-higgs-doublet models. *Physics Reports*, 516(1-2):1–102, 2012.
[22] Ilya F. Ginzburg and Maria Krawczyk. Symmetries of two higgs doublet model and *cp* violation. *Phys. Rev. D*, 72:115013, Dec 2005.
[23] The ATLAS Collaboration. Constraints on new phenomena via higgs boson couplings and invisible decays with the atlas detector. *Journal of High Energy Physics*, 2015(11), 2015.
[24] Sheldon L. Glashow and Steven Weinberg. Natural conservation laws for neutral currents. *Phys. Rev. D*, 15(7), 1977.
[25] M. Carena, S. Heinemeyer, O. Stå l, C. E. M. Wagner, and G. Weiglein. MSSM Higgs Boson Searches at the LHC: Benchmark Scenarios after the Discovery of a Higgs-like Particle. *Eur. Phys. J.*, C73(9):2552, 2013.
[26] M. Aoki, S. Kanemura, K. Tsumura, and K. Yagyu. Models of yukawa interactions in the two higgs double model, and their collider phenomenology. *Phys. Rev. D*, 80(1), 2009.
[27] Robert Harlander, Michael Kramer, and Markus Schumacher. Bottom-quark associated Higgs-boson production: reconciling the four- and five-flavour scheme approach. 2011. arXiv:1112.3478 [hep-ph].
[28] Lyndon Evans and Philip Bryant. Lhc machine. *Journal of Instrumentation*, 3(08):S08001, 2008.
[29] The ATLAS Collaboration. The atlas experiment at the cern large hadron collider. *Journal of Instrumentation*, 3(08):S08003, 2008.
[30] The CMS Collaboration. The cms experiment at the cern lhc. *Journal of Instrumentation*, 3(08):S08004, 2008.
[31] The LHCb Collaboration. The lhcb detector at the lhc. *Journal of Instrumentation*, 3(08):S08005, 2008.
[32] The alice experiment at the cern lhc. *Journal of Instrumentation*, 3(08):S08002, 2008.
[33] Cinzia De Melis. The CERN accelerator complex. Complexe des accélérateurs du CERN. Jul 2016. General Photo.
[34] The ATLAS Collaboration. https://twiki.cern.ch/twiki/bin/view/AtlasPublic/LuminosityPublicResults.
[35] The ATLAS Collaboration. https://twiki.cern.ch/twiki/bin/view/AtlasPublic/LuminosityPublicResultsRun2.
[36] Joao Pequenao. Computer generated image of the whole ATLAS detector. Mar 2008.
[37] G Aad et al. Atlas pixel detector electronics and sensors. *Journal of Instrumentation*, 3(07):P07007, 2008.
[38] Joao Pequenao. Computer generated image of the ATLAS inner detector. Mar 2008.
[39] M Capeans, G Darbo, K Einsweiller, M Elsing, T Flick,

M Garcia-Sciveres, C Gemme, H Pernegger, O Rohne, and R Vuillermet. ATLAS Insertable B-Layer Technical Design Report. Technical Report CERN-LHCC-2010-013. ATLAS-TDR-19, Sep 2010.

[40] The ATLAS TRT collaboration. The ATLAS TRT barrel detector. *Journal of Instrumentation*, 3(02):P02014, 2008.

[41] The ATLAS TRT collaboration. The ATLAS TRT end-cap detectors. *Journal of Instrumentation*, 3(10):P10003, 2008.

[42] M. Aharrouche et al. Energy linearity and resolution of the atlas electromagnetic barrel calorimeter in an electron test-beam. *Nuclear Instruments and Methods in Physics Research Section A: Accelerators, Spectrometers, Detectors and Associated Equipment*, 568(2):601 – 623, 2006.

[43] C et al. Adorisio. Study of the ATLAS MDT Spectrometer using High Energy CERN combined Test beam Data. *Nucl. Instrum. Methods Phys. Res., A*, 598(ATL-MUON-PUB-2008-005. ATL-COM-MUON-2007-013):400–415. mult. p, Nov 2007.

[44] Georges Aad et al. Measurements of the Total and Differential Higgs Boson Production Cross Sections Combining the $H \to \gamma\gamma$ and $H \to ZZ^* \to 4\ell$ Decay Channels at $\sqrt{s}$=8 TeV with the ATLAS Detector. *Phys. Rev. Lett.*, 115(9):091801, 2015.

[45] William Panduro Vazquez. The atlas data acquisition system: from run 1 to run 2. *Nuclear and Particle Physics Proceedings*, 273:939 – 944, 2016. 37th International Conference on High Energy Physics (ICHEP).

[46] Christoph et al. Eck. *LHC computing Grid: Technical Design Report. Version 1.06 (20 Jun 2005).* Technical Design Report LCG. CERN, Geneva, 2005.

[47] T Cornelissen, M Elsing, I Gavrilenko, W Liebig, E Moyse, and A Salzburger. The new atlas track reconstruction (newt). *Journal of Physics: Conference Series*, 119(3):032014, 2008.

[48] E. Bouhova-Thacker, P. Lichard, V. Kostyukhin, W. Liebig, M. Limper, G. Piacquadio, P. Lichard, C. Weiser, and A. Wildauer. Vertex Reconstruction in the ATLAS Experiment at the LHC. (ATL-INDET-PUB-2009-001, ATL-COM-INDET-2009-011), 2009.

[49] The ATLAS Collaboration. Electron efficiency measurements with the atlas detector using 2012 lhc proton–proton collision data. *The European Physical Journal C*, 77(3):195, Mar 2017.

[50] Estimation of non-prompt and fake lepton backgrounds in final states with top quarks produced in proton-proton collisions at $\sqrt{s} = 8$ TeV with the ATLAS detector. Technical Report ATLAS-CONF-2014-058, CERN, Geneva, Oct 2014.

[51] The ATLAS Collaboration. Measurement of the muon reconstruction performance of the atlas detector using 2011 and 2012 lhc proton–proton collision data. *The European Physical Journal C*, 74(11):3130, Nov 2014.

[52] W Lampl, S Laplace, D Lelas, P Loch, H Ma, S Menke, S Rajagopalan, D Rousseau, S Snyder, and G Unal. Calorimeter Clustering Algorithms: Description and Performance. Technical Report ATL-LARG-PUB-2008-002. ATL-COM-LARG-2008-003, CERN, Geneva,

Apr 2008.
[53] Matteo Cacciari, Gavin P. Salam, and Gregory Soyez. The anti-k_t jet clustering algorithm. *Journal of High Energy Physics*, 2008(04):063, 2008.
[54] Morad Aaboud et al. Jet energy scale measurements and their systematic uncertainties in proton-proton collisions at $\sqrt{s} = 13$ TeV with the ATLAS detector. 2017.
[55] Expected performance of the ATLAS b-tagging algorithms in Run-2. Technical Report ATL-PHYS-PUB-2015-022, CERN, Geneva, Jul 2015.
[56] The ATLAS Collaboration. Performance of missing transverse momentum reconstruction in proton-proton collisions at $\sqrt{s} = 7$ TeV with atlas. *The European Physical Journal C*, 72(1):1844, Jan 2012.
[57] The ATLAS Collaboration. The atlas simulation infrastructure. *The European Physical Journal C*, 70(3):823–874, Dec 2010.
[58] Torbjörn Sjöstrand, Stefan Ask, Jesper R. Christiansen, Richard Corke, Nishita Desai, Philip Ilten, Stephen Mrenna, Stefan Prestel, Christine O. Rasmussen, and Peter Z. Skands. An introduction to pythia 8.2. *Computer Physics Communications*, 191:159 – 177, 2015.
[59] T. Gleisberg, Stefan. Hoeche, F. Krauss, M. Schonherr, S. Schumann, et al. Event generation with SHERPA 1.1. *JHEP*, 0902:007, 2009.
[60] S. Agostinelli et al. GEANT4: A simulation toolkit. *Nucl. Instrum. Meth. A*, 506:250, 2003.
[61] G. Apollinari, O. Brüning, T. Nakamoto, and Lucio Rossi. Chapter 1: High Luminosity Large Hadron Collider HL-LHC. *CERN Yellow Report*, (arXiv:1705.08830. 5):1–19. 19 p, May 2017. 21 pages, chapter in High-Luminosity Large Hadron Collider (HL-LHC) : Preliminary Design Report.
[62] Letter of Intent for the Phase-I Upgrade of the ATLAS Experiment. Technical Report CERN-LHCC-2011-012. LHCC-I-020, CERN, Geneva, Nov 2011.
[63] ATLAS Collaboration. Letter of Intent for the Phase-II Upgrade of the ATLAS Experiment. (LHCC-I-023, CERN-LHCC-2012-022).
[64] ATLAS Phase-II Upgrade Scoping Document. Technical Report CERN-LHCC-2015-020. LHCC-G-166, CERN, Geneva, Sep 2015.
[65] The ATLAS Collaboration. Technical Design Report for the ATLAS Inner Tracker Strip Detector. Technical Report CERN-LHCC-2017-005. ATLAS-TDR-025, CERN, Geneva, Apr 2017.
[66] D Contardo, M Klute, J Mans, L Silvestris, and J Butler. Technical Proposal for the Phase-II Upgrade of the CMS Detector. Technical Report CERN-LHCC-2015-010. LHCC-P-008. CMS-TDR-15-02, Geneva, Jun 2015.
[67] M Shochet, L Tompkins, V Cavaliere, P Giannetti, A Annovi, and G Volpi. Fast TracKer (FTK) Technical Design Report. Technical Report CERN-LHCC-2013-007. ATLAS-TDR-021, Jun 2013. ATLAS Fast Tracker Technical Design Report.
[68] A. Annovi, M. M. Beretta, G. Calderini, F. Crescioli, L. Frontini, V. Liberali, S.R. Shojaii, and A. Stabile. Am06: the associative memory chip for the fast tracker in the upgraded atlas detector. *Journal of*

Instrumentation, 12(04):C04013, 2017.
[69] A. Annovi et al. A xor-based associative memory block in 28 nm cmos for interdisciplinary applications. *Proceedings of the International Conference on Electronics, Circuits, and Systems (ICECS)*, pages 392–395, 2015.
[70] The ATLAS Collaboration. Approved plots for the l1track trigger project. https://twiki.cern.ch/twiki/bin/view/AtlasPublic/L1TrackPublicResults.
[71] Mikael Mårtensson. Fast pattern recognition with the ATLAS L1Track trigger for the HL-LHC. *PoS(Vertex 2016)069*, 2016.
[72] ALEPH Collaboration, DELPHI Collaboration, L3 Collaboration, OPAL Collaboration, and The LEP working group for Higgs boson searches. Search for charged higgs bosons: combined results using lep data. *The European Physical Journal C*, 73(7):2463, 2013.
[73] Phillip Gutierrez. Review of charged Higgs searches at the Tevatron. *PoS*, CHARGED2010:004, 2010.
[74] The ATLAS Collaboration. Search for a light charged Higgs boson in the decay channel $h^+ \to c\bar{s}$ in $t\bar{t}$ events using pp collisions at $\sqrt{s} = 7$TeV with the ATLAS detector. *The European Physical Journal C*, 73(6):2465, Jun 2013.
[75] The CMS Collaboration. Search for a light charged Higgs boson decaying to $c\bar{s}$ in pp collisions at $\sqrt{s} = 8$TeV. *Journal of High Energy Physics*, 2015(12):1–37, Dec 2015.
[76] The ATLAS Collaboration. Search for a charged Higgs boson produced in the vector-boson fusion mode with decay $H^\pm \to W^\pm z$ using pp collisions at $\sqrt{s} = 8$TeV with the atlas experiment. *Phys. Rev. Lett.*, 114:231801, Jun 2015.
[77] The ATLAS Collaboration. Search for charged higgs bosons decaying via $h^\pm \to \tau^\pm \nu$ in fully hadronic final states using pp collision data at $\sqrt{s} = 8$ tev with the ATLAS detector. *Journal of High Energy Physics*, 2015(3):88, Mar 2015.
[78] Search for charged Higgs bosons in the τ+jets final state using 14.7 fb^{-1} of pp collision data recorded at $\sqrt{s} = 13$ TeV with the ATLAS experiment. Technical Report ATLAS-CONF-2016-088, CERN, Geneva, Aug 2016.
[79] The CMS Collaboration. Search for a charged higgs boson in pp collisions at $\sqrt{s} = 8$ tev. *Journal of High Energy Physics*, 2015(11):18, 2015.
[80] H. Georgi and M. Machacek. Doubly charged higgs bosons. *Nuclear Physics B*, 262(3), 1985.
[81] Andreas Crivellin, Ahmet Kokulu, and Christoph Greub. Flavor-phenomenology of two-Higgs-doublet models with generic Yukawa structure. *Phys. Rev.*, D87(9):094031, 2013.
[82] A. Arbey, F. Mahmoudi, O. Stal, and T. Stefaniak. Status of the charged higgs boson in two higgs doublet models. *arXiv:1706.07414v1 [hep-ph]*, Jun 2017.
[83] Torbjörn Sjöstrand, Stephen Mrenna, and Peter Skands. Pythia 6.4 physics and manual. *Journal of High Energy Physics*, 2006(05):026, 2006.
[84] F. Cascioli, P. Maierhöfer, and S. Pozzorini. Scattering amplitudes with open loops. *Phys. Rev. Lett.*, 108:111601, Mar 2012.

[85] Andreas Höcker, Peter Speckmayer, Joerg Stelzer, Jan Therhaag, Eckhard von Toerne, and Helge Voss. TMVA: Toolkit for Multivariate Data Analysis. *PoS*, ACAT:040, 2007.

[86] Glen Cowan, Kyle Cranmer, Eilam Gross, and Ofer Vitells. Asymptotic formulae for likelihood-based tests of new physics. *Eur. Phys. J.*, C71:1554, 2011. [Erratum: Eur. Phys. J.C73,2501(2013)].

[87] A L Read. Presentation of search results: the CLs technique. *Journal of Physics G: Nuclear and Particle Physics*, 28(10):2693, 2002.

[88] Céline Degrande, Maria Ubiali, Marius Wiesemann, and Marco Zaro. Heavy charged higgs boson production at the lhc. *Journal of High Energy Physics*, 2015(10):145, 2015.

[89] A. Elagin, P. Murat, A. Pranko, and A. Safonov. A new mass reconstruction technique for resonances decaying to $\tau\tau$. *Nuclear Instruments and Methods in Physics Research Section A: Accelerators, Spectrometers, Detectors and Associated Equipment*, 654(1):481 – 489, 2011.

Acta Universitatis Upsaliensis

Digital Comprehensive Summaries of Uppsala Dissertations from the Faculty of Science and Technology 1557

Editor: The Dean of the Faculty of Science and Technology

A doctoral dissertation from the Faculty of Science and Technology, Uppsala University, is usually a summary of a number of papers. A few copies of the complete dissertation are kept at major Swedish research libraries, while the summary alone is distributed internationally through the series Digital Comprehensive Summaries of Uppsala Dissertations from the Faculty of Science and Technology. (Prior to January, 2005, the series was published under the title "Comprehensive Summaries of Uppsala Dissertations from the Faculty of Science and Technology".)

Distribution: publications.uu.se
urn:nbn:se:uu:diva-329227

ACTA
UNIVERSITATIS
UPSALIENSIS
UPPSALA
2017